An Inverse Finite Element Method for Material Characterization of Small Hyperelastic Samples

by

Marga Christine Viljoen

Thesis presented in partial fulfilment of the requirements for the degree of Master of Engineering (Mechanical) in the Faculty of Engineering at Stellenbosch University

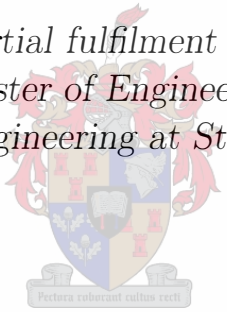

Supervisors:

Dr. J.H. Müller Prof. G. Venter

December 2019

Declaration

By submitting this thesis electronically, I declare that the entirety of the work contained therein is my own, original work, that I am the sole author thereof (save to the extent explicitly otherwise stated), that reproduction and publication thereof by Stellenbosch University will not infringe any third party rights and that I have not previously in its entirety or in part submitted it for obtaining any qualification.

Date: 2019/05/31 .....

UNIVERSITEIT·STELLENBOSCH·UNIVERSITY
jou kennisvennoot • your knowledge partner

Plagiaatverklaring / Plagiarism *Declaration*

1 Plagiaat is die oorneem en gebruik van die idees, materiaal en ander intellektuele eiendom van ander persone asof dit jou eie werk is.
Plagiarism is the use of ideas, material and other intellectual property of another's work and to present it as my own.

2 Ek erken dat die pleeg van plagiaat 'n strafbare oortreding is aangesien dit 'n vorm van diefstal is.
I agree that plagiarism is a punishable offence because it constitutes theft.

3 Ek verstaan ook dat direkte vertalings plagiaat is.
I also understand that direct translations are plagiarism.

4 Dienooreenkomstig is alle aanhalings en bydraes vanuit enige bron (ingesluit die internet) volledig verwys (erken). Ek erken dat die woordelikse aanhaal van teks sonder aanhalingstekens (selfs al word die bron volledig erken) plagiaat is.
Accordingly all quotations and contributions from any source whatsoever (including the internet) have been cited fully. I understand that the reproduction of text without quotation marks (even when the source is cited) is plagiarism.

5 Ek verklaar dat die werk in hierdie skryfstuk vervat, behalwe waar anders aangedui, my eie oorspronklike werk is en dat ek dit nie vantevore in die geheel of gedeeltelik ingehandig het vir bepunting in hierdie module/werkstuk of 'n ander module/werkstuk nie.
I declare that the work contained in this assignment, except where otherwise stated, is my original work and that I have not previously (in its entirety or in part) submitted it for grading in this module/assignment or another module/assignment.

Studentenommer / *Student number*	**Handtekening / *Signature***
Viljoen MC **Voorletters en van / *Initials and surname***	December 2019 **Datum / *Date***

Abstract

The aim of this research was to develop and test an experimental method, which could be scaled to samples of 4 mm x 4 mm x 1-2 mm in size. To validate the design of the experimental method, it was applied to samples (10 mm by 10 mm by 2.5 mm in size) of a soft hyperelastic silicone-rubber using available equipment.

The biggest challenge in this research was the small scale at which testing was performed. In addition, the size of force measurements was small (under 10 N), which meant that force measurements inherently included noise, which could not be neglected.

The method was designed such that stress concentrations were avoided and boundary conditions were simple enough to be easily implemented in a finite element analysis. A uni-axial compression test was performed where full-field displacement data was measured using digital image correlation and force data was measured using a 50 N load cell. Displacement and force results for compressions of between 20-55 % of the height of the sample were used in an inverse finite element model updating method to iteratively determine a three parameter Mooney-Rivlin material model for the hyperelastic silicone-rubber.

There was a large amount of variability in the force results, even though the displacement inputs for the tests were repeatable. The inverse finite element model updating method showed repeatability in the value to which it converged, however the material model obtained from the optimization process produced accurate displacements neither when plotted against the experimental displacements nor when implemented in a validation test geometry.

Uittreksel

Die doel van hierdie navorsing was om 'n eksperimentele metode, wat geskaal kan word na monsters van 4 mm x 4 mm 1-2 mm, te ontwikkel en te toets. Om die ontwerp te toets, is die metode toegepas op monsters (10 mm by 10 mm by 2,5 mm in grootte) gemaak van 'n sagte hiper-elastiese silikoon-rubber deur gebruik te maak van beskikbare toerusting.

Die grootste uitdaging in hierdie navorsing was die klein skaal waarby toetse uitgevoer is. As gevolg daarvan, was die grootte van gemete kraglesings klein (onder 10 N), wat beteken het dat resultate geraas ingesluit het, wat nie weglaatbaar klein was nie.

Die metode is op so manier ontwerp dat spanningskonsentrasies vermy is en randvoorwaardes eenvoudig genoeg was om maklik in 'n eindige element analise geïmplementeer te word. 'n Eenassige druktoets is uitgevoer waar volveldverplasingdata gemeet is deur digitale beeldkorrelasie en kraglesings geneem is met behulp van 'n 50 N lassel. Verplasings en kragte vir vervormings van tussen 20-55 % van die hoogte van die monster is gebruik in 'n inverse eindige element model opdateringsmetode om die konstantes van 'n drie-parameter Mooney-Rivlin materiaal model vir die hiper-elastiese silikoon-rubber te bepaal.

Daar was 'n groot mate van variasie in die kraglesings, alhoewel die verplasingsinsette herhaalbaar was. Die inverse eindige element model opdateringsmetode het herhaalbaar tot dieselfde waarde konvergeer, maar die materiaalmodel wat uit die optimeringsproses verkry is, het onakkurate verplasingswaardes voorspel vir beidie die experimentele geometrie en die validasie toets.

Contents

List of Figures

List of Tables

Nomenclature

Abbreviations

DIC	Digital Image Correlation
DOF	Depth of Field
FE	Finite Element
FEA	Finite Element Analysis
FEM	Finite Element Model
FL	Focal Length
FOV	Field of View
HFD	Hyperfocal distance
OD	Object Distance
RMSE	Root Mean Square Error
SBT	Soft Biological Tissue
UTM	Universal Testing Machine
WD	Working Distance

Variables

A	Projected Width of Sample	[mm]
AR	Aspect Ratio	[ ]
B	Projected Depth of Sample	[mm]
$C10$	Mooney-Rivlin Constant 1	[ ]
$C01$	Mooney-Rivlin Constant 2	[ ]

$C11$	Mooney-Rivlin Constant 3	[ ]
CoC	Size of the Circle of Confusion	[mm]
d	Displacement	[mm]
D_{far}	Furthest extremity of DOF	[mm]
D_{near}	Closest extremity of DOF	[mm]
d_s	Diagonal Size of Sensor	[mm]
DOF	Depth of Field	[mm]
F	Force	[N]
FL	Focal Length	[mm]
FOV	Diagonal Size of FOV	[mm]
f_{stop}	Aperture	[ ]
HFD	Hyperfocal Distance	[mm]
L	Length	[mm]
OD	Object Distance	[mm]
P_a	Size of a Pixel (in a-direction)	[mm]
$sample_x$	Width of Sample	[mm]
t	Time	[s]
x	X-coordinate	[mm]
y	Y-coordinate	[mm]
z	Z-coordinate	[mm]
ϕ	Aspect Ratio Angle	[°]
θ	Half Stereo Angle	[°]

Subscripts

x, y, z	Coordinates

Chapter 1

Introduction

This project originated out of a need to test the material properties of very small heart valve tissue samples. The size and nature of these samples present a problem: testing slippery, hyperelastic samples at such a small scale is practically difficult.

The aims of this project have been set up to use the equipment and technology available at Stellenbosch University to test an experimental method for determining the material properties of elastic material samples at a reachable scale. The research will serve as a proof of concept for the experimental method. In this section, the problem statement, project aims, and project objectives are discussed.

1.1 Problem Statement

Studying the deterioration of biological replacement heart valves, after they have been implanted in an *in vivo* model for some time, is an important factor for improving the designs of these valves, but samples from explanted valves are very small (4 mm x 4 mm x 1-2 mm). Experimental methods that aid in determining the material properties of very small elastic material samples would enable researchers to determine more accurate material models for these materials and to model the deterioration of the biological materials used in the construction of biological replacement valves.

However, testing at this small scale would present some serious challenges:

1. It is hard to grip such small samples due to spatial constraints.
2. The material is slippery and very elastic. For accurate measurements, it is vital that the sample must not slip in the test setup during testing.
3. The small size and elasticity of the samples introduces challenges in terms of measuring strain and limits the strain measurement options.

4. Stress concentrations and gripping effects in a sample of this size would dominate the strain field.

5. Specialized lenses for measuring strain using digital image correlation (DIC) would be needed at a scale of 4 mm.

At the time of doing this research, the appropriate equipment for measuring at a 4 mm scale was not available to the researcher.

The proposed research involved designing and testing an experimental method, which would enable future researchers to determine the material properties of very small (4 mm x 4 mm x 1-2 mm) hyperelastic samples. The method would be tested at a scale that enabled the use of the equipment that was available to the researchers at the time of experimentation.

1.2 Aims

The aim of this research is to develop an experimental method to test the material properties of hyperelastic material samples, which are small in size. Even though the method developed could be applicable to fields outside the study of biological tissues, the design process should take into account that the original intent was to improve the methods available for testing biological materials. This means that the design of the experimental protocol should take into consideration what the desired scale of observation for testing biological samples will be in future research.

Special consideration should be given to improving the method where conventional methods of testing fall short. Especially in terms of preventing stress concentrations and/or gripping effects, slipping of the sample during testing and reducing the scale at which experimentation is possible.

1.3 Objectives

The following objectives are identified in order to fulfil the project aims.

1. Profile the ability of available equipment to determine the smallest scale possible for testing at Stellenbosch University. Since the biological samples that this method is being developed for will pose challenges in terms of the scale of experimentation it would not be appropriate to test the method at a scale that eliminates these challenges.

2. Design a viable experimental method for testing small (4 mm) samples, which improves upon the shortcomings of current standard testing procedures for biological samples. Especially in terms of avoiding stress concentrations, gripping effects, and slip.

3. Develop the experimental protocol for the proposed method of testing and implement this method in physical tests. The development of the experimental method should take into consideration the ease of post-processing of the acquired data.

4. Develop the numerical procedure for post-processing of the experimental data to calculate the material model for the tissue. This includes setting up multi-disciplinary software interactions to implement the FEM update method.

5. Evaluate the experimental protocol as a workable method to test the material properties of small hyperelastic samples and in terms of its viability for testing heart valve tissue. A workable method would be usable for testing biological tissue at a 4 mm scale. The method should produce results that are both accurate and reliable and the resulting material model must be usable in FEA.

1.4 Project Scope

Since this research originated from the need to test small biological material samples it must keep in mind the limitations and challenges of testing the specific type of biological samples as explained in the problem statement. However, since the availability of these samples is limited, instead it was decided to test on a hyperelastic silicone-rubber material to evaluate the experimental method designed in the research.

The following is included in the scope for this project:

1. Choose the material model and optimization algorithm for the FEM update method from literature.

2. Design the experimental geometry according to the objectives set out for this project.

3. Choose the most appropriate available equipment and quantify the variability in measurements.

4. Set up a finite element model (FEM) for the experimental geometry. This includes performing a mesh refinement study and choosing appropriate boundary conditions.

5. Implement the FEM model and experimental results in the FEM update method to calculate a material model.

6. Do a validation test using the material model obtained from experimentation in a different test geometry to test the success of the model obtained in (5).

The following is excluded from the scope

1. Procurement of equipment.
2. Testing different optimization algorithms and material models.
3. The goal of this research is not to completely characterise the material, but rather to calculate a simple material model, which enables researchers to model the material deformation in FEM. Testing other material attributes like compressibility, strain hardening, and stress relaxation is not in the scope for this research.

The required measurement accuracies will be defined in Section 3.2.1.

Chapter 2

Background

This chapter provides background information on the concepts, methods, and materials used in this project, as well as considerations necessary when working at a scale of 4 mm. An overview of heart valve replacements is presented to provide background to the motivation behind this research. The properties of soft biological tissue (SBT) and the methods for testing such materials are explained based on previous studies. This section also discusses material models for tissue and soft elastomers before Section 2.6 explains digital image correlation (DIC) and the theory involved in designing a DIC experiment for a specific specimen size. Lastly, the inverse finite element model (FEM) update method is explained.

2.1 Heart Valve Replacements

When the need arises to replace natural structures in the body (like heart valves) it can be difficult to find materials which are able to perform well in comparison to the native tissues. There are a lot of factors to consider when choosing these materials. When patients suffer from valvular heart disease, a common solution is to replace the diseased valve with a prosthetic heart valve (Jiang *et al.*, 2005).

There are two common types of replacement heart valves: (1) mechanical replacement valves and (2) bioprosthetic replacement valves (also referred to as tissue valves) (Hamid *et al.*, 1985). Bioprosthetic replacement heart valves come in many different forms, but this research is focused on stented bioprosthetic heart valves. The valves differ in terms of their construction, the method of implantation, the materials they are made out of and their life cycles. Two important factors need to be considered when selecting a valve type.

Firstly, to prolong the lifetime of a valve under *in vivo* conditions, the material has to be durable. Natural heart valve tissues can repair themselves, which bio-

prosthetic replacement heart valves cannot do (Legg *et al.*, 2012). In terms of this first consideration, mechanical replacement valves typically perform much better than the currently available bio-prosthetic replacement valves (Welt *et al.*, 2012).

Secondly, valve material must be compatible with the body in terms of both bio-compatibility and biomechanics. In other words, how closely the replacement material can mimic the functionality of the native tissue. Bioprosthetic valves are the superior choice in terms of both bio-compatibility and flow behaviour (Legg *et al.*, 2012; Cupido *et al.*, 2016). The trileaflet design of bioprosthetic valves is similar in geometry to that of the native heart valve, and the flow of blood through the valve more closely resembles the flow through a native valve, (Yoganathan *et al.*, 2004). Patients with mechanical implants have to take anticoagulant medication for the remainder of their lives since the turbulent flow patterns in these valves could cause thromboembolisms (Legg *et al.*, 2012). These advantages of bio-prosthetic replacement heart valves make it worthwhile to investigate the possibility of increasing their durability through design.

2.2 Stented Bio-prosthetic Replacement Heart Valves

Bioprosthetic heart valves consist of three leaflets attached to a scaffold or a stent. The leaflets are made of biological materials like bovine, sheep or kangaroo pericardium, or porcine valve leaflets. The design mimics the anatomy of a native heart valve more closely, as the trileaflet design is closer in geometry to that of a native human heart valve and the material of the valve more closely mimics the biomechanics of native heart valve tissue. For these reasons, bio-prosthetic replacement valves offer the advantage over normal mechanical replacement heart valves that the patient does not have to be on anticoagulants, or even a special diet, for the rest of their life (Tillquist and Maddox, 2011).

A further advantage of bioprosthetic replacement heart valves is that the leaflets can also be attached to a stent. Stented bioprosthetic heart valves can be implanted by performing a transcatheter valve replacement, which is less invasive and less time consuming than open-heart surgery. This procedure can be performed on patients who cannot undergo open heart surgery because it is too much of a risk, and for whom a valve replacement would be impossible by any other method (Kheradvar *et al.*, 2015).

As mentioned before, the biggest downfall of bioprosthetic valves is that they are less durable than mechanical heart valves. As time passes, the biological materials of the valve leaflets degenerate, which often results in the need for

re-operation. As a result, bioprosthetic heart valves are usually only chosen over mechanical valves if the patient is older than 60 years, because it can be assumed that the patient will not outlive the life expectancy of the valve (Kheradvar *et al.*, 2015). This means a large percentage of people who receive heart valve replacements still receive mechanical valves and must make significant lifestyle changes in addition to taking anticoagulant medication for the remainder of their lives. Although the durability of bioprosthetic heart valves has improved, it is still inferior to the durability of mechanical valves (Kheradvar *et al.*, 2015).

The lack in material models of both intact and bioprosthetic heart valves complicates the improvement of current designs. Without accurate material models to describe the behaviour of the material, designs cannot be accurately modelled and validated in terms of leaflet dynamics as well as valve lifetimes.

The challenge with finding material models is that the materials used to construct bioprosthetic valves have complex stress-strain behaviours and it is physically difficult to test and derive material models that describe their stress-strain behaviour accurately (Kheradvar *et al.*, 2015; Yoganathan *et al.*, 2004). The complex nature of tissue as a material and the structural properties thereof are discussed in the next section.

2.3 Material Characteristics of Soft Biological Tissues

Soft biological tissues (SBT) and cells inherently exhibit complex behaviour, because of their complex microstructure (Humphrey, 2003). Soft tissues do not obey Hooke's law (Wertheim, 1847; Roy, 1880), where displacement is correlated to the applied force using the elastic modulus. Instead, they undergo large non-linear deformations at small stresses or forces (Vito, 1980).

SBT can be considered as anisotropic, viscoelastic, nonlinear and heterogeneous, and the material properties vary with a multitude of external and internal variables like the time after excision, excision itself, the age of the donor, the gender of the donor, and disease (Roy, 1880; Humphrey, 2003; Lanir, 1982). Internal variables are structural differences between different samples. One of the internal variables that influence the behaviour of these materials is the fibre structure of the specific type of tissue. SBT consist of a large percentage of collagen and elastin proteins, which are responsible for the interesting mechanical behaviour observed, because these tissues act like elastomers consisting of crosslinked fibres (Pioletti, 2000). Different tissues, with different functions and mechanical requirements, have different fibre distributions (orientation and concentration) and fibre characteristics (length and thickness) in order to perform their required function in the body (Lanir, 1982). All of

these parameters may cause variations in the properties between two samples or even local variations within one specimen.

Lastly, the viscoelastic behaviour of SBT makes it even more complex, since it is dependent on time (in terms of creep and stress relaxation) and strain rate (Panda and Buist, 2018). The viscoelasticity of tissue is attributed to its high water content, which means that it creeps under a constant load, shows hysteresis when cyclically loaded, and undergoes stress relaxation under constant displacement (Humphrey, 2003).

The mechanical behaviour of skin tissue under a uniform strain rate can be divided into three phases and research related the observed behaviour to the underlying structure of the biological material (Figure 2.1). There is an initial phase of extension as the collagen fibres start to align (1), whereafter there is a phase of stiffening due to the fibres being aligned (2). Finally, when the individual fibres start to break, yielding occurs (3). This behaviour was characterised by Ridge and Wright (1965, 1966*b*,*a*).

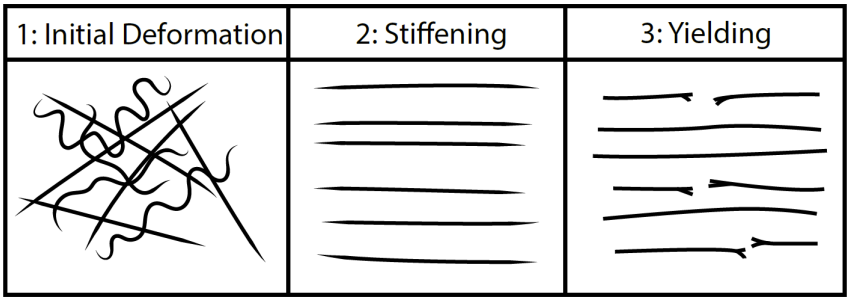

Figure 2.1: Fibre Configurations for Three Phases of Deformation

Intrinsic material properties like yield strength and ultimate tensile strength are not expected to vary with sample size, but it has been found that strain measurements on SBT vary greatly dependent on the length of the biological sample (Sanjeevi *et al.*, 1982). In addition, gripping mechanisms often result in irregular, non-uniform strain fields, which can greatly influence measurements and cause variability in the material behaviour observed (Sun *et al.*, 2005; Jimenez *et al.*, 1989). Additionally, uneven sample shapes like dumbells, have an unknown effect on the behaviour of the material, since the fibres contribute largely to material behaviour (Anssari-Benam *et al.*, 2012).

2.4 Material Testing of Soft Biological Tissues

Veronda and Westmann (1970) found, in uni-axial experiments on cat skin, that the tissue was incompressible, non-linear and anisotropic, however, they suggested that an isotropic approximation of the material's behaviour showed

good correlation with experimental results. The research suggested that the properties of tissue should be tested by means of a bi-axial test or more complex induced strain fields because the material is anisotropic and a one-dimensional tensile test would measure the properties for only one direction. Fung made a similar statement in 1973 when he identified a need for the development of constitutive equations from multiaxial loading conditions for the general behaviour of tissue under stress and strain. The importance of a complex deformation field is further highlighted by Vito (1980), who noted that three-dimensional constitutive equations cannot be determined from the results of one-dimensional experiments.

Tissue samples are usually small, especially samples from human heart valves, and the material is slippery. The first consideration makes it is difficult to fix the material to the experimental setup such that there are no stress concentrations affecting the results at the point of measurement. Many studies fix specimens to experimental setups using hooks (Cabrera *et al.*, 2013) or sutures (Strumpf *et al.*, 1993), but this method of constraining the sample introduces stress concentrations in the form of holes (discontinuities) that may affect the accuracy of the results, especially if the sample is small. Other methods of constraining the sample include clamps, ball screws (Vito, 1980) or freezing the sides of the sample to the test setup. These methods will be physically challenging to execute in a test at the 4 mm sample size available in this study.

Adverse effects of stress concentrations can be avoided if measurements are taken at a point where the influence of the stress concentration has decayed. Measurements taken within the region of the characteristic decay length of these effects will be erroneous, which complicates testing on 4 mm samples (Anssari-Benam *et al.*, 2012). Figure 2.2 shows the influence of stress concentrations using the example of hooks.

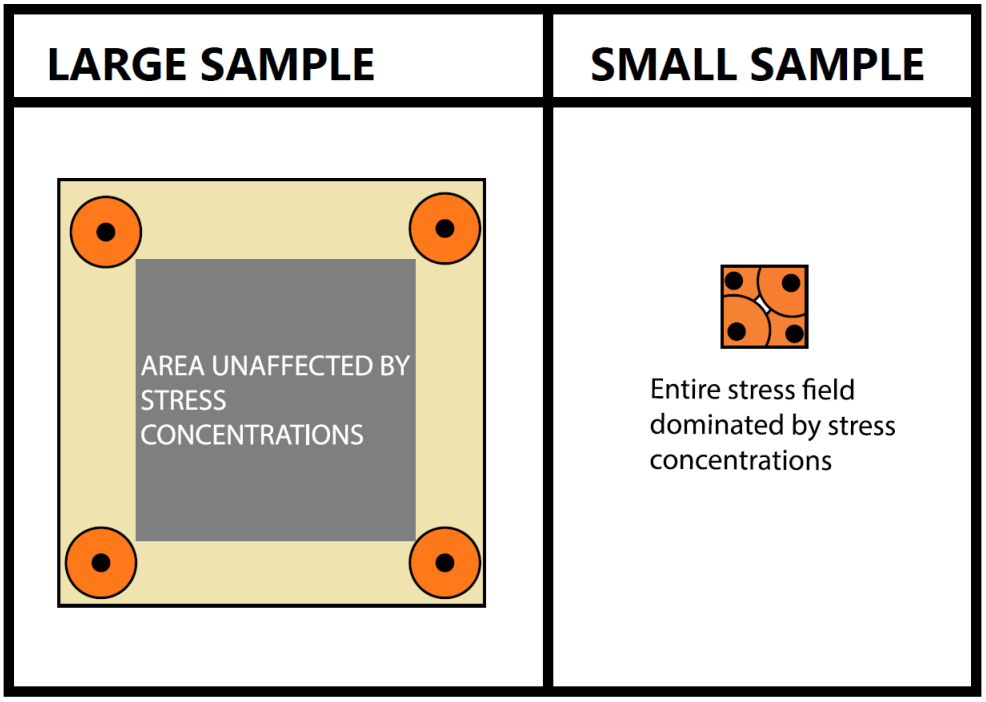

Figure 2.2: Effect of Stress Concentrations on a 4 mm Sample with Holes

2.5 Material Models for Soft Biological Tissues

Models for the material behaviour of SBT's remain lacking, even though tremendous progress has been made towards this goal (Humphrey, 2003). The problem with available data for the mechanical properties of the construction materials for bioprosthetic heart valves is that samples are difficult to test on because it is difficult to fix biological materials to an experimental setup (Pioletti, 2000). The standard for testing the material properties of a new material is to use a dumbbell shaped sample in a stretch test. This method works well for metals and softer materials but requires the sample to be a specific size. The understanding and modelling of the mechanisms of tissue failure are not as developed as the theory of fracture mechanics of engineering materials, and there is a need to better understand the mechanics of tissue failure, especially under complex, dynamic loading conditions (Humphrey, 2003). As stated before, SBT does not obey Hooke's law and more complex material models are needed to model their behaviour.

A review article by Humphrey (2003) identified five steps in the process of deriving a constitutive equation for a material:

1. Delineate the general characteristics which are of interest.

2. Determine the appropriate theoretical framework to characterise the material's behaviour.

3. Identify the specific form of the constitutive equation which is appropriate for the application.

4. Calculate the values of the chosen parameters from experimental data.

5. Validate the results from (4) to determine the performance of the predictive model.

Two common approaches for deriving constitutive equations which predict material behaviour are thermodynamic equations and structural equations. Thermodynamic equations consider the value of the total strain energy to be equal to the sum of the strain energies of the different components of a material. Structural theories depend on the functions and structures of the different components of a material, which means that the material model will be clear in terms of relating parameters back to the physical properties of the tissue (Lanir, 1982).

The study of tissue biomechanics has the potential to help optimize the design of medical procedures and devices in order to improve the quality of life of many people globally (Humphrey, 2003) by improving the base of knowledge and the theoretical frameworks for predicting and modelling the behaviour of different tissues. According to a workgroup in 2002 (reported by Humphrey (2003)), important research avenues in biomechanics include the need to develop an accurate understanding of how tissues react to stresses and how they heal, fatigue and fail. The improvement of material data is only possible with development in the experimental procedures and material models used to describe the material.

In the developmental phase of an experimental method, it is advisable to validate the method using a surrogate material. Especially in cases where the material in question is expensive to procure. Advances in tissue biomechanics usually follow advances in the experimental methods and constitutive equations for elastomers (Humphrey, 2003), since both polymers and soft biological tissues (SBT) have long, chain-like, cross-linked microstructures, they exhibit some characteristics which are similar (nonlinear, incompressible, viscoelastic) (Treloar, 1975; Martins *et al.*, 2006). According to Humphrey (2003) and Martins *et al.* (2006), the biggest difference between these materials (in terms of behaviour) is that rubbers are usually isotropic, while most tissues behave as anisotropic materials. This anisotropic behaviour varies for different types of tissue, due to the differences in the function and structure of the tissues.

Hooke's law is inappropriate to use for the description of the behaviour of silicone-rubber during deformation (Mooney, 1940; Rivlin, 1948). Rubbers are

usually modelled using constitutive equations. It was found by Panda and Buist (2018) that nonlinear models for rubbers were unable to predict the behaviour of soft tissues accurately, but in a study by Martins *et al.* (2006) it was found that the Mooney-Rivlin model could be implemented in an inverse FEM update method, where a correlation coefficient (between experimental data and FEA output) of 0.99755 was achieved for a soft silicone-rubber and 0.99659 for soft tissue. This specific study implemented the two-variable version of the Mooney-Rivlin model and the optimizer converged within three iterations. It was found that the strain rate dependency of soft unfilled silicone-rubbers is negligible and that the Mullins effect may be ignored (Meunier *et al.*, 2008).

The Mooney-Rivlin model has a high accuracy for predicting the behaviour of nonlinear, isotropic, rubber-like materials (Martins *et al.*, 2006). Hyperelastic models perform better when applied to rubber-like materials than to tissues (Martins *et al.*, 2006). The Mooney material model is most commonly used for describing the properties of elastomers because it is simple and it represents the behaviour of this type of material well for moderate deformations (Meunier *et al.*, 2008). It has long been implemented in commercially available FEA software along with some other hyperelastic models (like Ogden or the Neo-Hookean model). The three parameter Mooney-Rivlin material model is shown in Equation 2.1 (Kumar and Rao, 2016). Some models, like the Ogden Model, have more parameters than the Mooney-Rivlin model, which means that more variables need to be optimized when it comes to inverse method and solution times may increase (Meunier *et al.*, 2008).

$$S = C_{10}(\lambda - \frac{1}{\lambda}) + 2C_{01}(1 - \frac{1}{\lambda^3}) + 6C11(\lambda^2 - \lambda - 1 + \frac{1}{\lambda^2} + \frac{1}{\lambda^3} - \frac{1}{\lambda^4}) \quad (2.1)$$

2.6 Digital Image Correlation (DIC)

There are a few ways in which strain can be measured. Digital image correlation (DIC), is a non-contact, full-field method of measuring strain or displacements. This method measures the deformation of the sample surface using an optical analysis. Digital correlation methods have been shown to produce accurate results for measuring displacements, but large variability for directly computing strains. It is possible to measure displacements corresponding to strains of up to 200% as well as small strains at an accuracy of between a 20th and a 100th of a pixel with the out of plane displacement measurements being the least accurate (Reu, 2012*b*).

2.6.1 DIC as a Strain Measurement Method

In DIC the deformation of a sample is tracked using calibrated photographic images. Since it is an optical method, the scale of observation at which DIC

is performed can be from nanoscopic to macroscopic (Besnard *et al.*, 2006).

Strains are measured by correlating images taken after deformation to a reference image taken before deformation using a random grey level (speckle pattern) on the surface of the sample. A speckle pattern must be applied to the surface if the material is naturally free from features (Vacher *et al.*, 1999).

Images are divided into grid elements with uniform dimensions. Each corner of each grid element forms a point and an area with variable dimensions is formed around each point, which is used to identify a unique grey level correlation pattern. Points are located in the deformed image, using a correlation coefficient to find the matching grey level in each correlation pattern of the deformed shape (Sutton *et al.*, 1986). More detailed information regarding the numerical optimization methods and interpolation used to calculate displacements is available in a paper by (Sutton *et al.*, 1986). In Sutton's paper an optimized digital correlation method is proposed which uses a second-order optimizer (Newton-Rhapson Method) with differential correction. Second-order methods are the fastest but may have convergence problems, which Sutton's method improved on.

The average displacement of an element in the image is related to a physical displacement measurement using calibration information from the DIC software (Vacher *et al.*, 1999). Figure 2.3 shows the concepts discussed in this paragraph.

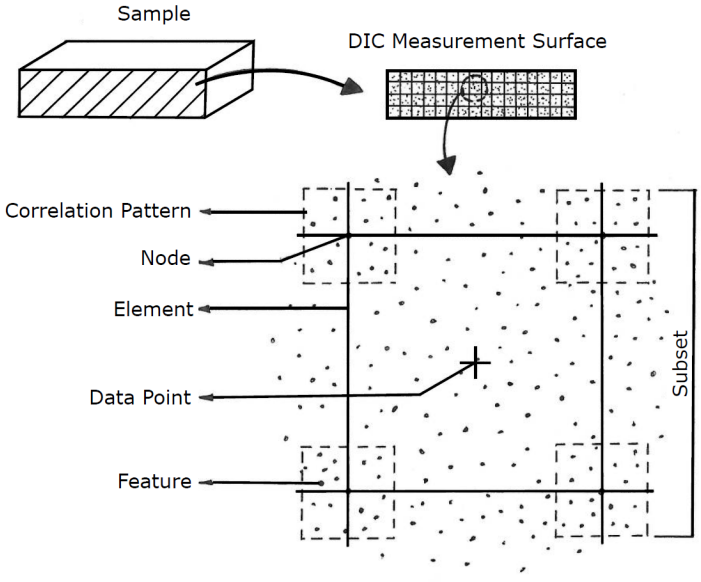

Figure 2.3: Definitions of DIC Concepts

Figure 2.4 shows an element on the sample surface with a correlation pattern around each node.

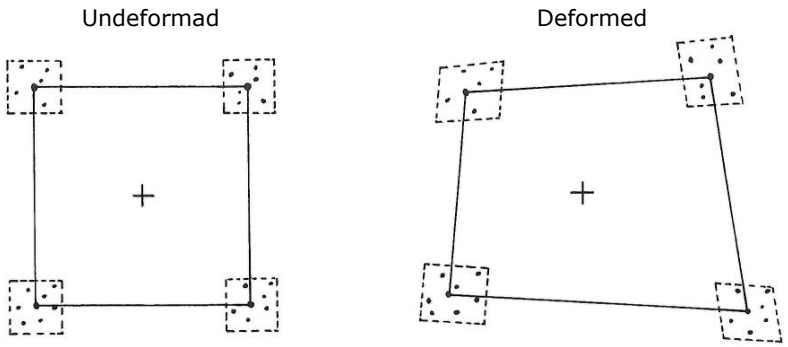

Figure 2.4: Using Correlation to Find Deformation

To successfully complete digital image correlation, there are some major requirements to be met at all times (Reu, 2012*b*,*a*, 2013*a*,*c*,*b*).

1. The sample must be in focus for the duration of deformation and the area being monitored must be as close to the centre of the field of view of the camera as possible.

2. The sample must be within the frame at all times.

3. The sample must be well illuminated and the area where measurements are taken should be covered with a completely random speckle pattern with high contrast. Features should be smaller than 20 pixels Vacher *et al.* (1999) and subsets must be at least 30 pixels in size. The pattern must be neither too sparse (too few features) or too dense (too many features overlap) (GmbH, n.d.; LePage, 2018).

4. The DIC setup must remain completely still to maintain the accuracy of equipment calibration during testing.

5. The textural quality of the image must be high, as it will have a large effect on the quality of the measurements taken.

Please refer to (LePage, 2018) for examples of proper speckle densities.

2.6.2 DIC Setup

A complete 3-dimensional DIC setup consists of two cameras, a tripod (for stability), a controller, and a light source. The nature of the setup is dependent on the requirements for the measurement of strain in the specific experiment.

For three-dimensional displacement measurements, images from both cameras are superimposed to calculate deformations in the third direction, which is perpendicular to the lens. The cameras should be placed at a half stereo angle of 15-35° relative to each other (Figure 2.5). The larger this angle, the more accurate out of plane measurements will be, which will correspond to a loss in the accuracy of in-plane measurements (Reu, 2013*c*).

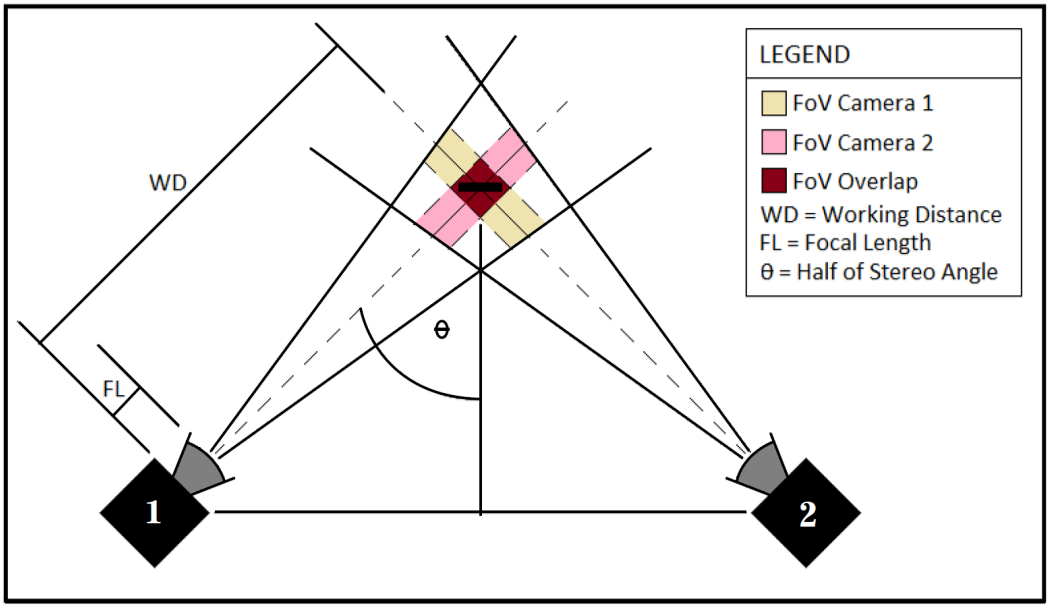

Figure 2.5: Field of View

The second consideration is lighting. Lighting is important to ensure a high contrast image with proper exposure (Reu, 2012*a*). Over- or underexposure will prevent the DIC software from identifying features since detail and contrast of the speckle pattern are lost (Besnard *et al.*, 2006).

A third requirement is a stable surface, preferably, a tripod for the equipment to rest on. This gives greater freedom to manoeuvre the lights and cameras to the desired position while providing the necessary stability once the system is calibrated (Reu, 2012*b*). Any slight movement of the equipment would require recalibration of the entire setup.

The lenses are the last important consideration for a complete DIC setup. Lenses are responsible for scaling the camera's field of view to the scale of

observation needed for the experiment. This aspect of the DIC system is what lends itself to its scalability.

2.6.3 Lens Selection

To tailor a DIC system to the scale of observation for a specific experiment, the correct set of lenses must be chosen. In order to understand the lens selection criteria, the principle behind camera focus must be explained.

The object distance of a lens is defined as the distance from the camera sensor to the object as shown in Figure 2.6. A camera achieves perfect focus when the object distance is at the focal point of the lens. However, there is a margin before and after the focal point where the focus of the image is acceptable. This is known as the depth of field (DOF). For a DIC experiment to be successful, the sample must fall within the depth of field for the entire deformation process.

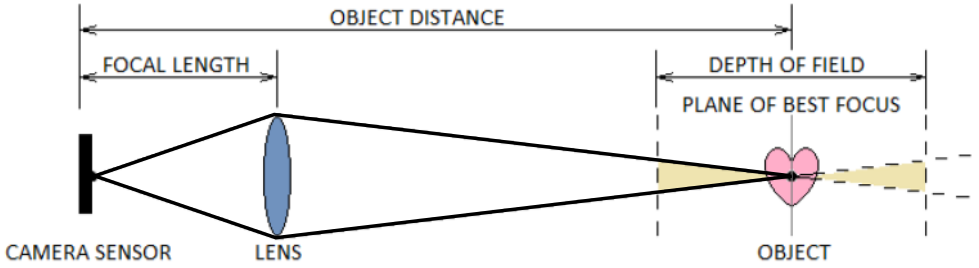

Figure 2.6: Depth of Field

There are three variables that influence the DOF: the focal length, the object distance and the aperture of the lens. Table 2.1 shows a summary of how an increase or decrease in any of these variables will influence the DOF.

Table 2.1: Effects of Camera Variables on Depth of Field, (Reu, 2013*a*)

	Depth of Field	
Variable	Increase	Decrease
Focal Length	Shorter	Longer
F-Stop number	Larger	Smaller
Object Distance	Longer	Shorter

When two cameras are used to measure strain in three dimensions, the field of view (FOV) and DOF of both cameras must overlap for the DIC software to successfully capture sample deformation. This further reduces the area within which the sample may deform while maintaining accurate strain measurements

as shown in Figure 2.5. The required lens specifications are calculated from the required scale of observation.

For the sake of brevity, the equations used to select the proper lens set are discussed in Appendix A.1. Implementation of these equations in the design of the experimental setup is discussed in Chapter 3.

2.6.4 Calibration

A DIC setup must be calibrated to the size of the FOV in physical space. To do this, an image (or multiple images) of an object, with markers of a known dimension, spaced at a predefined distance, is taken. Usually, the object is a plate, with very precise markings on its surface, called a calibration plate. These plates can be created in the DIC software and printed out to scale on paper (Figure 2.7).

Two-dimensional calibration plates are defined by four parameters: the size of the plate, the size of the markers, and the distance between markers in both the x- and y- directions. Figure 2.7 shows these values on an example of a calibration plate.

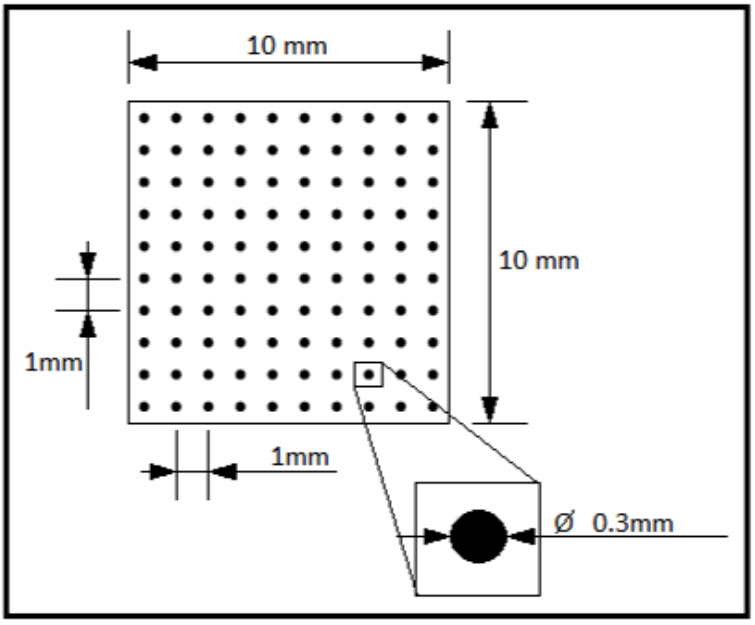

Figure 2.7: Example of a Calibration Plate With Four Defining Parameters

A two-dimensional calibration plate has to be rotated a few times and photographed in multiple (at least eight) orientations to calibrate the out of plane direction. The dots on the surface of the calibration plate are identified by the software and the calibration for the set up is then computed from these images.

Calibration for DIC systems is dependent on the aperture and focal length of the lenses, the distance from the camera to the sample, and the stereo angle of the cameras. At a small FOV, DIC calibration accuracy is lost if any of these values are slightly changed or disturbed (Reu, 2012*b*).

2.7 Non-Linear Finite Element Modeling

2.7.1 Non-Linear Finite Element Analysis

A FEM problem can be non-linear due to three types of non-linearities: geometric non-linearity, material non-linearity and contact.

Geometric nonlinearities include large deformations and rotations, preloads and structural instabilities like buckling. Material nonlinearities include phenomenon where the behaviour of the material changes significantly with the applied load. This may include creep and strain hardening among other things. Lastly, contact is nonlinear because the material will behave differently in the region of contact than it normally would mar.

MSC Marc and Mentat is an implicit non-linear Finite Element Analysis (FEA) solver. Mentat may be seen as the user interface of the software. It requires user input and is the space where the model is defined (geometry, loads, materials etc.). The simulation parameters like parallel processing and solver methods are also defined here. When the simulation is then started Mentat passes the user inputs (.dat file) to Marc, which is the computational side of the software. Marc iteratively computes the FEA results using the user inputs from Mentat. During this phase of the simulation, there is no user input and the results are passed back to Mentat in a results file. These results are then read by Mentat and the user can plot and export them using the graphical user interface. Mentat also supports the use of procedure files to receive user input using code (mar).

Marc can solve hyperelastic models, which model the behaviour of polymers. It also supports different element types, all of which are able to handle large deformations. A material is hyperelastic when it exhibits highly elastic and nonlinear stress-strain behaviour. These types of materials remain elastic up to very large strain values (sometimes more than 100%).

2.7.2 Large deformation modeling of Hyperelastic Materials

Material models for hyperelastic materials are usually based on the strain energy function. A commonly used hyperelastic model, which is well implemented in Finite Element Software is the Mooney-Rivlin model Swanson *et al.*

(1985). The Mooney-Rivlin model is based on right Cauchy-Green stress invariants and is able to model large deformations. Another hyperelastic model, the Ogden model uses principal stretch ratios in the strain energy function, which makes it less convenient for FE simulationsSwanson *et al.* (1985).

Zisis *et al.* (2015) used investigated the Mooney-Rivlin model as well as other material models and found that similar results were obtained.

2.8 Finite Element Model Update Method

The FEM update method is a numerical method through which data from a DIC experiment is used to optimize the material constants in a finite element model (FEM) of the experimental geometry, such that the FEM output matches the experimental data. This is especially useful in cases where materials exhibit complex behaviours.

Anisotropic material responses are inherently direction dependent. A deformation field with both compressive and tensile directional strains could potentially result in a material model that is applicable to a wider range of load cases when using the FEM update method (Garbowski *et al.*, 2012)

2.8.1 Summary of the FEM Update Method

Figure 2.8 shows the inverse FEM update method as a process flow diagram.

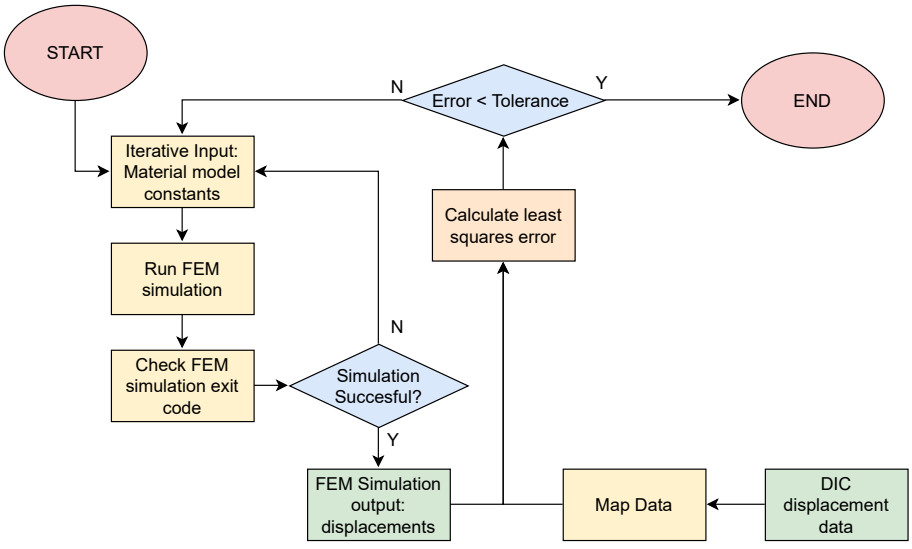

Figure 2.8: Inverse FEM Update Method - Process Flow

Comparison of the experimental results to the results from the FEA requires that the geometry, boundary conditions, and initial conditions are consistent between the experiment and the simulation. First, an initial estimate of the material properties is made and implemented in the FEM. Next, the FEM simulation is executed to find the theoretical deformation of the sample according to the initial estimate of the material model. The output from the FEM simulation, for this research, is the deformation field for the sample according to the guessed material model. Finally, the FEM output is compared to the experimental data in order to determine if the material model accurately predicted the material behaviour.

FEM output data is given at the locations of the nodes in the FEM whereas DIC data is known at each DIC element location. To compare these datasets, data points from one data set must be mapped over to corresponding initial locations in the other data set. For this step, a surface fit is applied to either the DIC experimental data (as shown in this section) or to the FEM output, where the displacement of each element in x, y and z can be calculated as a function of its initial position in x and y as shown in Equations 2.2 , 2.3 and 2.4 respectively.

$$f(x_{iDIC}, y_{iDIC}) = \delta x_{DIC} \tag{2.2}$$
$$g(x_{iDIC}, y_{iDIC}) = \delta y_{DIC} \tag{2.3}$$
$$h(x_{iDIC}, y_{iDIC}) = \delta z_{DIC} \tag{2.4}$$

$f(x_{iDIC}, y_{iDIC})$, $g(x_{iDIC}, y_{iDIC})$ and $h(x_{iDIC}, y_{iDIC})$ are the surface fits in the x, y and z-directions, respectively, and δx_{DIC}, δy_{DIC} and δz_{DIC} represent the experimental data for the displacement of the sample in the three directions.

Since the FEM model is very similar to the actual experimental geometry, the initial x- and y-positions on the surface of the sample and the surface of the FEM model are comparable with each other and the surface fits obtained from equations 2.2 to 2.4 can be used to determine what the displacement of each node in the FEM model should be according to the experimental data. In other words, Equations 2.2, 2.3 and 2.4 are applied to the initial positions of each node in the FEM model to obtain their predicted displacements as shown in Equations 2.5 , 2.6 and 2.7.

$$\delta x_{MAP} = f(x_{iFEM}, y_{iFEM}) \tag{2.5}$$
$$\delta y_{MAP} = g(x_{iFEM}, y_{iFEM}) \tag{2.6}$$
$$\delta z_{MAP} = h(x_{iFEM}, y_{iFEM}) \tag{2.7}$$

Where δx_{MAP}, δy_{MAP} and δz_{MAP} give the values for the displacement of each FEM node (in all three directions) as predicted by experimental data.

The next step is to calculate the root mean square error (RMSE) between the experimental data and the FEM output by using equations 2.8 to 2.11. This value is used to determine whether the guessed material parameters results in behaviour similar to that observed in the experimental results and it will be used as the objective function for the inverse FEM update method. The goal of the simulation is to iterate material properties until the error value is either zero or smaller than a chosen tolerance value.

ϵ is the RMSE value that compares the results from the FEM simulation to the experimental data. δx_{FEM}, δy_{FEM} and δz_{FEM} are the displacement output values for each node in the FEM simulation in the x-, y- and z-directions respectively and n is the number of nodes.

$$\epsilon = \frac{\sum_{i=0}^{n} \sqrt{\epsilon_{x,i}^2 + \epsilon_{y,i}^2 + \epsilon_{z,i}^2}}{n} \tag{2.8}$$

$Where$

$$\epsilon_x = \delta x_{MAP} - \delta x_{FEM} \tag{2.9}$$

$$\epsilon_y = \delta y_{MAP} - \delta y_{FEM} \tag{2.10}$$

$$\epsilon_z = \delta z_{MAP} - \delta z_{FEM} \tag{2.11}$$

The implementation of data mapping is discussed in Section 4.3.3.

This method of finding material parameters allows for the use of complex material models, which would be challenging to define using explicit methods. It also allows for the use of samples with unconventional shapes and allows researchers to develop material testing beyond the usual tensile test. The drawback of using optimization as a tool to find material parameters is that it is a black box solution. In other words, it is possible to find a material model that describes the behaviour of a material very well in simulations, but there is no deeper knowledge regarding which parameter corresponds to which material characteristic or structure. The constants in the material model carry no information regarding the material itself, but it can predict the material response for applied initial and boundary conditions.

Another problem is that iterative methods use a lot of computational power, especially when running a FEM update method since it means that an iterative process (solving of a FEM simulation) is taking place within each iteration of the optimizer. This can add up to long solution times and a simulation which is very computationally expensive to run.

Ultimately, the FEM update method is the only realistic way to find a material model from experimental results (in this case) and it can be used to produce

accurate results for both silicone-rubber and soft tissue (Martins *et al.*, 2006; Meunier *et al.*, 2008). The most applicable material models for these materials are usually constitutive black box equations instead of more straightforward structural equations usually applicable to metals.

2.8.2 Numerical Optimization

Numerical optimization is an iterative process through which the optimal inputs for a cost function is found. The cost function is usually a function of one or more variables. The goal is to find the values for these variables, which result in the optimum value for the cost function. This may be either a minimum or a maximum value of the function (Beers, 2006).

Say the cost function is defined as F(x, y, z). In an unconstrained optimization x, y, and z may have any real values, however, if there is a predefined range within which these values must fall, the problem is a constrained optimization.

In gradient methods, optimization is applied by means of evaluating the gradient of the cost function. The next iteration in the values of x, y and z is then made in the direction of the steepest gradient. In other words, the direction in which the value of F will change the most in the favourable direction with a change in the values of x- y- and z. These methods are efficient, but large steps in the values of the variables may lead to the optimization overshooting the local minimum or maximum value of F (Beers, 2006).

For this research, the modified method of feasible directions was used as the optimization algorithm as suggested by Jekel *et al.* (2016). This method is a gradient-based optimization method and is implemented in the optimization software for constrained optimization problems.

The method of feasible directions (MFD) is a gradient-based optimization algorithm, which may be used for non-linear optimization problems. It calculates a search direction vector as well as a step size and is suitable for constrained problems (Chang *et al.*, 2005). In addition, the Modified Feasible Direction method takes into account the direction of the previous iteration (Topal and Uzman, 2008).

If any constraints are violated at any point, the algorithm will deem the solution non-viable and will then find a search direction back into the feasible domain of the problem. If the solution is within the feasible domain the optimizer will continue until convergence is reached (Chang *et al.*, 2005). This may be defined as a point where the absolute or relative difference between two points is smaller than a specified tolerance value and the solution complies to all constraints (Topal and Uzman, 2008).

2.8.3 Optimization Software

DOT (Vanderplaats Research and Deveopment, Inc) is an abbreviation for Design Optimization Tools. It is a software package which is used to perform numerical optimization calculations. A cost function is defined along with its input variables (Research and Development, 2008).

In addition to the definition of the inputs and cost function in DOT, there is also a solver needed to calculate the value of the cost function for each set of input values of the variables. Code may be written in DOT to calculate the value, or the software may be linked to external solvers. If the software is linked to an external solver DOT will iterate values for the input variables, which are then implemented in the external solver. When this solver calculates the value of the costing function it is returned to DOT where it is used to determine the values of the variables in the next iteration until the value of the cost function converges to either a minimum or maximum value. DOT may be implemented using code or by the use of the graphical user interface, VisualDOC (Vanderplaats Research and Deveopment, Inc), but the operating principle remains the same.

Since DOT evaluates the values of the cost function numerically, there is no gain in the understanding of the mechanics of the cost function's behaviour. It is a 'black box solution', meaning that the software has knowledge of only the input and output values. However, the solution may be used to find the optimum solution for the defined problem. In the case of this research, the solution gives the material model variables which produce the behaviour closest to measured experimental outputs. In this way, it is possible to find an accurate material model without knowing the mechanics behind the observed behaviour.

2.9 Available Materials and Equipment

For this project, the idea was to develop the experimental method using available and accessible technology to mitigate costs. Strain would be introduced by means of a compressive force on the sample. A universal testing machine (UTM) was chosen for this application because it had a small enough resolution in terms of the displacement increments of the crosshead.

Two universal testing machines (UTM) were available. The specifications of these machines are compared in Table 2.2. Machine (B) (MTS Criterion 44) has a smaller displacement resolution, but the smallest allowable load cell for this machine has a rating of 1 kN, which was much larger than the expected maximum force. Since the samples in this research project were very small and soft in comparison to conventional material testing, the displacement accuracy of the crosshead had to be as fine as possible and the load cell had to be as small

as possible. Option (A) (Instron 3345) had a larger displacement resolution, but it could use a load cell with a rating of 50 N.

The resolution for a load cell was estimated as 0.5 % of its rating, which translates to 0,25 N in the case of the 50 N load cell and 5 N for the 1 kN load cell. Measurements smaller than this value can be seen as noise. Since the maximum amount of compressive force expected in these experiments would be lower than 30 N it was best to use the 50 N load cell even though it would not be possible to synchronise the DIC and UTM measurements automatically. Otherwise the measurement of force would be lost in the measurement noise.

Table 2.2: Comparison of Available UTM Equipment

UTM Make and Model	(A)	(B)
Displacement Resolution (nm)	133	49
Force Capacity (kN)	5	30
Force Accuracy (% of Rating)	0.5	0.5
Minimum Allowable Load Cell Capacity (N)	50	100
Minimum Available Load Cell Capacity (N)	50	1000
Internal DAQ timer	No	Yes

As discussed in section 3.3, the strain measurements for this project could only be done using DIC. The available DIC setup consisted of a tripod, two cameras with a set of lenses, two LED light sources, a processing unit and a computer (Figure 2.9). The tripod ensured stability during filming so that the data would not be compromised by movement of the camera. If the camera moved at all during testing, the calibration would become invalid for the data captured after the disturbance, as discussed in Section 2.6.4. The lenses on the DIC system determined the smallest scale at which deformation could be measured.

Figure 2.9: DIC Setup (Viljoen)

Four sets of lenses were available for the DIC setup. The specifications for these lenses are summarised in Table 2.3. The lens properties determined how suited each lens set was for the required application. The final set of lenses was chosen based on the smallest achievable scale of observation as discussed earlier in this chapter.

Table 2.3: Specifications of Available Lens Sets

Lens Set	1	2	3	4
Focal Length [mm]	85	75	18 - 180	35
Maximum Sensor Size [mm]	11.06	6	11.06	11.06
Minimum F/Stop	1.8	4	2	1.6
Maximum F/Stop	16	30	18	16
Special Features	N/A	Double Gauss Focus-able	Zoom Lens	TV Lens

The DIC LED light sources ensured that the sample would be properly illuminated to ensure that the captured images were neither too dull nor too bright since both extremes would cause a loss in contrast between the speckle pattern and the background (Reu, 2013*b*). The cameras for the DIC setup were industrial black and white cameras (Imager E-Lite 5M, LaVision GmbH). Colour was not necessary for this method and it would, in fact, lower the effectiveness of the system (Reu, 2012*a*).

Chapter 3

Experimental Design

In this research, an alternative experimental method of testing the material properties for small samples was explored. The specialised equipment and material preparation techniques needed to test at a 4 mm scale would be expensive. Therefore, the proposed method was tested using a surrogate material (which is inexpensive in comparison to biological samples) and the scale was limited to the smallest sample size achievable using the available resources. The study may be seen as a validation of the experimental method to motivate possible expenses for future research and the goal for this experiment is to determine whether or not the method itself has the potential to improve current material data. The experiments may, therefore, be seen as a proof of concept.

This chapter explains the design choices made for this research, from concept generation to detail design, after which specifications for the final experimental equipment design are reported.

Design development started with a functional decomposition of the design, before generating concepts using a morphological analysis. Concept generation was focused on the different functions involved in testing material properties: inducing strain, measuring strain, and measuring applied force. The concept generation was somewhat limited, by the available equipment, in terms of the smallest achievable scale of observation, but not in terms of the concept design itself.

3.1 Functional Decomposition

The first design step was to do a functional decomposition of the experimental design. A functional decomposition is an analysis of the design problem, where it is decomposed into its required functions (Blanchard and Fabrycky, 1990). For this project the functional decomposition started with the most basic functional requirement of the system: the method must test the material

properties of small elastic material samples. The functional decomposition is shown in figure 3.1 below.

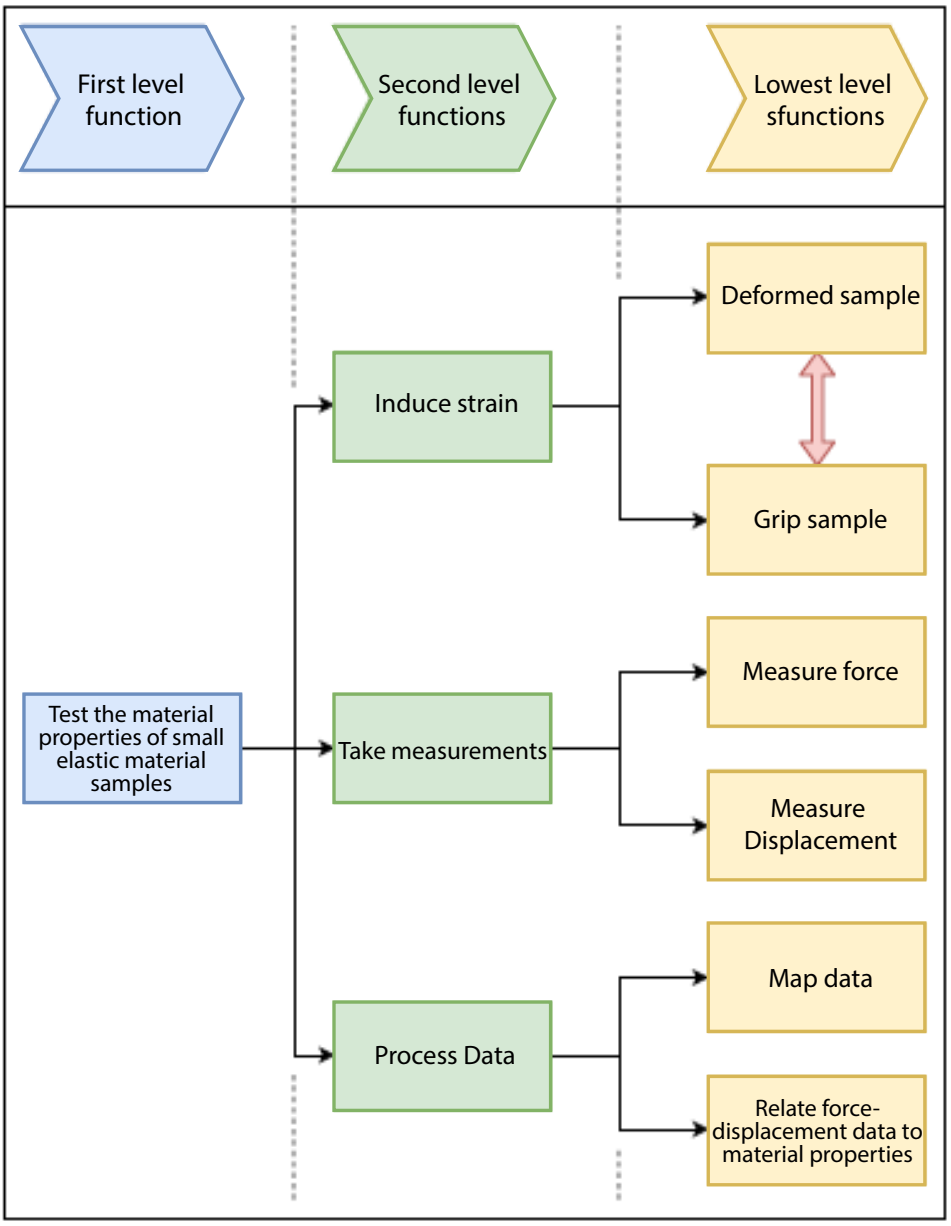

Figure 3.1: Functional Decomposition

To achieve the first level function the sample must be positioned, gripped and deformed, and environmental conditions must be relatively constant to ensure repeatability. The deformation of the sample and the force corresponding to

the deformation must be measured and material constants must be calculated by implementing these measurements in an inverse FEM update method.

Once the functional decomposition of the design was completed, a morphological chart of the design options for each function was made and different options were evaluated using the design requirements.

3.2 Concept Generation

This section describes how a morphological chart was implemented to choose the appropriate components for each part of the experimental design. A morphological chart was used to identify and evaluate different options for fulfilling each function identified in the functional decomposition (Pahl, 2001). Different concepts were generated by combining options from each category before each concept was evaluated in terms of how well it fulfilled the design objectives. The best solution was chosen as the final conceptual design.

3.2.1 Design Requirements

The design objectives are discussed in Section 1.3. These were translated to the design requirements listed below. These requirements served as a guide to designing the experimental method as they formed the criteria for selecting a final design as discussed in Section 3.2.2.

Design Requirements:

1. The experimental method must not cause stress concentrations in the sample during experimentation in order to accommodate for the small scale of testing desired.

2. It must be possible to implement the physical test at a 4 mm scale.

3. The method must be scalable to samples of 4 mm x 4 mm x 1-2 mm. To keep the method as close to this ideal as possible it should be designed in such a way that a scale of no more than three times the desired scale is achieved. In other words: the final sample size must be smaller than 12 mm x 12 mm x 3-6 mm.

4. The method of measurement should not affect material behaviour, or any effect must be known with reasonable accuracy, such that the error introduced due to this effect is smaller than 1%. Non-contact methods are preferable above contact methods.

5. The sample must have a complex strain field where individual directional strains include areas of both compression and extension. This is advan-

tageous when using the FEM update method as explained in chapter 2.

6. Data from the tests must be usable for inverse FEM update methods. The format must be readable by the software used to implement the numerical optimization. Data must include at least three different magnitudes of input force and at least 500 data points.

7. The test geometry must be duplicable in a robust finite element model (FEM), which can be to tailored to experimental geometries and inputs. A robust finite element model will be defined here as a model which converges for various different values of the material constants in order to be usable for the FEM update method.

8. The results must be validated. The material model obtained from testing should predict the deformation of the material (amount of strain for a corresponding input force) with an error of less than 10% for the results to be considered favourable (This gives an indication of accuracy). To test reliability The values measured for force should fall within 10% of the full-scale force value and the results from the FEM update method should converge to the same values (±5%). Correlation must be at least $R^2 = 0.95$.

Although it is important to validate the results this requirement is not included in the design process, because it does not influence the design of the test method. However, it is an important step in evaluating the success of the method and Section 3.6 is a summary of the validation method used

The next section explains how these requirements were implemented in a morphological analysis.

3.2.2 Morphological Analysis

The morphological chart was generated by exploring different design options for each function discussed in the functional decomposition. Table 3.1 was set up with possible solutions to each function. This table shows options which were found to be unviable in the specific application highlighted in grey.

Then, four different combinations of these options were generated as possible concepts for the design. Two of these options were not viable, therefore only the two most promising options are discussed in the section on concept selection. The two design options which were viable are shown in

During this design process, it was found that the design options would be limited in terms of the measurement of strain and force. It was found that digital image correlation (DIC) is the only viable means of measuring strain

Table 3.1: Functions and Possible Solutions

Functions				
Grip Sample (F1)	Deform Sample (F2)	Measure Force (F3)	Measure Displacement (F4)	Post Processing (F5)
Solutions				
Hooks	Bi-axial tensile load	Weights	Strain guage	Implicit solution
Clamps	Uni-axial tensile load	Load Cell	Extensometer	Explicit Solution
Sutures	Uni-axial compressive load		Digital Image Correlation (DIC)	
Freeze sample to equipment	Bi-axial load, sample attached to larger base.			
Constrain with rough surface				

and a load cell would be the best way to measure the applied force. The morphological analysis of these two functions is discussed below, while the functions of gripping and deforming the sample are discussed in 3.3.

Strain gauges and extensometers are used widely in applications where the material properties of hard materials, like metals and composites, need to be determined, but because of practical considerations, they were not suited for the application explored in this project. The most important considerations were size, ease of attachment to a surface, the compatibility of the sample material with the material of the strain gauge and the number of dimensions considered in the measurements taken.

The third option was to measure deformation using DIC. As discussed in section 2.6, DIC is an experimental method where the deformation of a sample is tracked using calibrated photographic images. This method can track strain in three dimensions and it can be tailored to almost any scale of observation using appropriate lenses. There is no contact between the equipment and the sample, meaning deformation of the sample is not affected by the method of measurement.

To measure the corresponding force exerted on a sample, either a force measurement device is needed or the applied force must be otherwise known. Using weights with a known size was considered, but it was decided that the measurement of force using a load cell would be much easier to implement since a universal testing machine (UTM) was chosen for applying a load. Furthermore, the accuracy of force measurements would be higher when using a load cell.

CONCEPT 1			
F1	**F2**	**F3**	**F4**
Clamps	Bi-axial Tensile Load, sample attached to larger base	Load Cell	DIC
Advantages		**Disadvantages**	
Sample free from stress concentrations Practical test size may be chosen Scalable to 4mm x 4mm x 1mm		Complex Post-Processing Complex modeling Multiple unknown variables (especially with regards Two-dimensional deformation Simple deformation field (tensile only) Slippage is a possibility	
CONCEPT 2			
F1	**F2**	**F3**	**F4**
Constrain with rough surface	Uni-axial compressive load	Load Cell	DIC
Advantages		**Disadvantages**	
Sample free from stress concentrations due Three Dimensional Strain Field Three Dimensional Strain measurements Simple modeling Relatively simple post-processing Non-contact measurement of strain Scalable to 4mm x 4mm x 1 mm Areas of both compression and tension.		Test size is sample size	

Figure 3.2: Viable Concepts for Experimental Method

These machines may be fitted with various types of grips and platforms and they are able to exert either a tensile or a compressive force in one direction. They usually have excellent displacement control and may be fitted with various sizes of load cells to cater to the specific experiment.

In the next section, concept selection is explained in terms of the design functions for which more than one viable design option was available.

3.3 Concept Selection

As explained in the literature review, the traditional method of testing the material properties of tissue has been bi-axial tensile testing, but in the case of this research, it was not practical. An alternative method for introducing strain had to be used.

Two viable concepts were generated using the morphological chart. These concepts are shown in Figure 3.3. Figure 3.2 shows a summary of advantages

and disadvantages of each concept.

The first concept (Figure 3.3 (A)) was to fix the sample to a base material with properties very close to that of tissue. This base material would have to be well studied and the material model of the heart valve tissue would be determined using the difference in behaviour of the base material when the tissue sample was introduced. The base would be a similar size as usually used in bi-axial tension tests. This way a bi-axial test could be used to study the material properties of the tissue, however there would be some complications when using this approach.

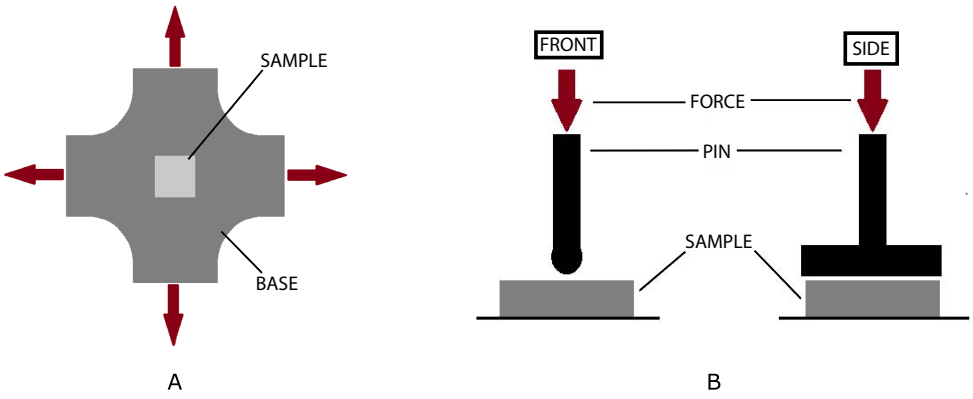

Figure 3.3: Viable Generated Concepts: Concept 1 (A) and Concept 2 (B)

It would be difficult to model the interface between the base material and the sample in a finite element simulation. Furthermore, the availability of accurate bi-axial testers is limited. Lastly, this method would analyse the material using two-dimensional plane strain assumptions instead of a three-dimensional deformation field.

The second concept (Figure 3.3 (B)) was analogous to an indentation test. The sample would be placed on a flat surface (baseplate) and compressed by a pin in order to produce a complex 3D strain field. Figure 3.4 shows a simulation of what the resulting deformation field might look like.

It may be seen in the figure that the deformation would result in a bulge on the front surface of the sample with deformations in all three cartesian directions. In addition to this three dimensionality it was also expected that there would be a difference in directionality of the strains in different directions: there would be tensile strains in the x- and z-directions and compressive strain in the y-direction.

The second method eliminated the problems caused by the introduction of stress concentrations as no holes or tears would be introduced into the sample

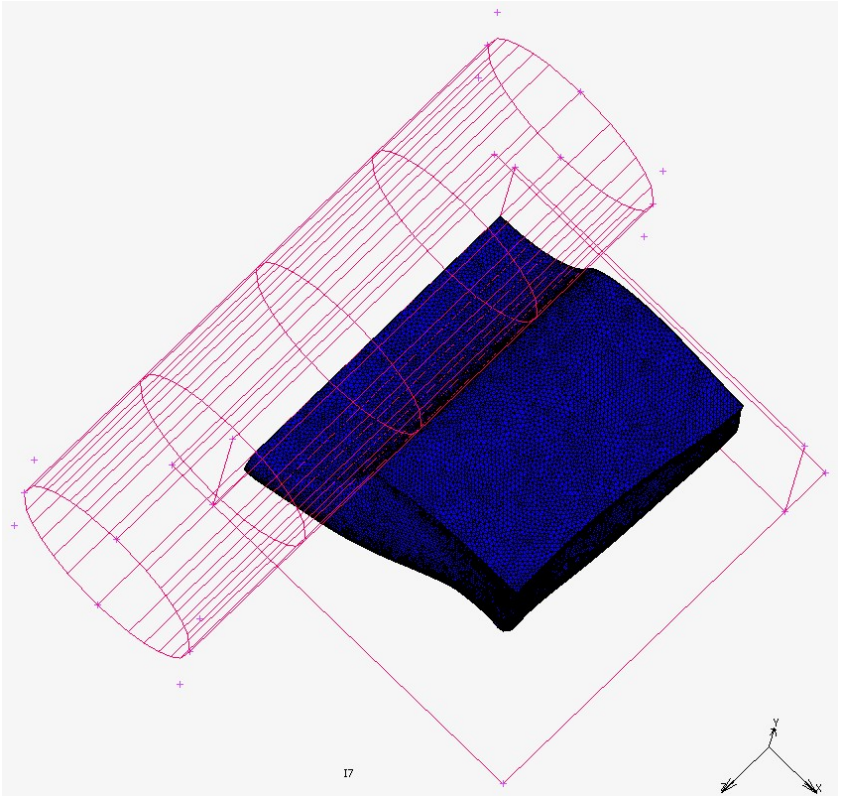

Figure 3.4: Deformation Field

and it would not be clamped. The boundary conditions for such a strain field would be easier to model, as there are be no practical issues with gripping the sample in clamps and no uncertainty due to slipping of the sample. The biggest challenge with this method was trying to keep the sample from slipping on the base plate. Fortunately, this could be easily overcome by placing the sample on a rough material such as sandpaper.

Neither plane stress nor plane strain could be assumed using this method because a complex deformation field would be produced. The deformation would have to be monitored in three dimensions, but the geometry of the sample was simple and the boundary conditions were easy to implement in a finite element simulation.

The evaluation of each concept, in terms of the requirements in section 3.2, is shown in table 3.2. The last requirement was not evaluated in this table, because the validation of the results does not depend on the design and will be a different experiment. It was decided that concept B was the superior choice since it performed best at satisfying the design requirements.

Table 3.2: Evaluation of Concepts According to Requirements

DESIGN REQUIREMENT	**CONCEPT**	
	A	**B**
No Stress Concentrations are introduced	1	1
Test is possible at 4 mm scale	1	1
Test Sample Size Smaller than 12 mm	1	1
Method of Measurement Does not Affect Results	1	1
Deformation is Complex	0	1
Data Usable in Inverse FEM Update Methods	1	1
Geometry of Sample is Easily Replicable in FEM	0	1
Total	5	7
KEY:	1 = Requirement is Met 0 = Requirement is not Met	

3.4 Detail Design

As discussed in Section 2.6.3, the selection of lenses is one of the most crucial aspects of designing a DIC experiment. The chosen lenses and lens settings determine the size of the field of view (FOV) and the depth of field (DOF) for the DIC process.

The first step in selecting a lens set for this project was to compare all of the available lenses in terms of both the size of their smallest possible field of view as well as the depth of field that could be achieved at that scale. The lenses listed in Table 2.3 were evaluated.

Table 3.3 shows the calculated field of view (FOV) and the corresponding depth of field (DOF) for each lens set. The values were calculated using equations A.1 to A.5 in Section 2.6.3, for the lens specifications in Table 2.3. An object distance of 500 mm was assumed since it would be large enough for the tripod to be mounted and close enough to keep the FOV as small as possible during testing. A camera angle of 30 degrees was assumed. This angle would ensure that out of plane measurements were as accurate as possible, while being small enough to not compromise the in-plane resolution (Reu, 2013*c*). Appendix A.2 shows a detailed sample lens calculation, as it was implemented for one lens set.

The aim of the researcher was to use the smallest possible field of view for the experimental setup, in order to test the smallest possible sample size. For this reason, the first and last lens sets in Table 3.3 were eliminated as possible design choices. Samples had to be as small as possible, but the camera lens had to be able to provide a depth of field big enough for the sample to deform freely, without images of it going out of focus.

Lens set 2 (TECHSPEC® Focusable Double Gauss Imaging Lenses, Edmund

Optics) was able to produce the smallest FOV, corresponding to the largest relative DOF between the remaining options.

Table 3.3: Field of View and Depth of Field for available Lens Sets

Lens Set	1	2	3	4
Minimum Focal Length (mm)	85	75	18	35
Maximum Focal Length (mm)	85	75	180	35
Minimum F/Stop	1.8	4	2	1.6
Maximum F/Stop	16	30	18	16
Total DOF (mm)	6.75	9.07	4.44	44.69
Field of View (mm)	64.8	40	51	157.37

After the appropriate lens set was chosen, it had to be further investigated to ensure that the image quality could satisfy the requirements for a successful DIC analysis. As discussed in Chapter 2, checks have to be implemented to ensure that the sample will be in full focus even maximum deformation and the pixel density on the surface of the sample must be sufficient to ensure that many DIC data sets (of 30 pixels each) can be identified. The values in table 3.4 were calculated using equations A.6 to A.14 as explained in Section 2.6.3. It is important to remember these values are calculated for one camera in order to include the effects of the stereo angle.

The first check verified if the depth of field would be large enough for the sample to be in focus even at maximum deformation. A minimum allowable sample size of 10 mm x 10 mm x 2.5 mm was assumed following the calculated FOV for the chosen lenses.

It was assumed that the depth of the sample (projected to the plane of the camera) in the undeformed state was a good indication of whether the depth of field of these lenses was adequate. This value was defined as the depth of half the sample as seen by the camera. In other words, how big must the depth of field be for the sample to be completely in focus when it is undeformed. This value was found to be 2.5 mm which was less than half the

Table 3.4: Final Checks for Lens Selection

Lens Property	Value	Unit
ϕ	39.8	Degrees
Frame Width	30.73	mm
Frame Height	25.61	mm
Pixel Width	0.0109	mm
Pixel Height	0.0125	mm
Number of Pixels in Width	796.69	number of pixels
Number of Pixels in Height	400.32	number of pixels
Depth of Sample in Undeformed State	2.5	mm

value of the calculated DOF. Thus, the depth of field would be adequate for the deformation of the sample.

For subset sizes of 30 pixels each, as suggested by Reu (2012*b*) (in other words six in the width and five in the height of each subset), it was found that the pixel density was adequate because the surface of the sample could be divided into over 100 subsets in the width and about 80 subsets in the height. In general, the more DIC elements, the more data is available for the optimizer. Over 8000 data points would be adequate experimental data for a DIC experiment, even if this theoretical approximation was not reached in reality.

It is important to note that even though these calculations give an indication of whether or not this DIC setup could capture data at the scale required, the setup in real life would not necessarily produce the predicted number of data points. This was due to the fact that a DIC system is set up by hand and has to be adjusted for many factors that will only be known on the day of experimentation. There would also be some deviation with regards to setting up the equipment, as detailed in the calculations, on account of human error. For this reason, the researcher had to ensure that the system could, in theory, achieve more than was required by the design.

3.5 Quantification of Variability

Two quantifiable variables were identified as possible contributors to variability in the experimental data: (1) stress relaxation of the material

3.5.1 Displacement Accuracy

To verify the accuracy of the UTM displacement measurements, the displacement of the pin during experimentation was measured using DIC and a comparison was made to the values reported by the UTM machine.

The error between the two values was then calculated. Since the values reported from both the DIC software and the UTM machine are given terms of relative position, it was decided to compare the displacement values in stead. The UTM is set up to move in increments of 0.2 mm at a time, but it is necessary to check the actual displacement values as a way of checking whether the machine is properly calibrated.

The test was repeated three times. Table 3.5 shows the values for displacement from both DIC measurements and the UTM output. The average absolute relative error between the two measurements was 3.55%.

Table 3.5: Comparison of Displacement Values from DIC Results and UTM Measurements

Test No.	UTM Step [mm]	DIC Step [mm]	Absolute Relative Error [%]
1	-0.2	-0.1903	4.85
2	-0.2	-0.1972	1.4
3	-0.2	-0.1912	4.4

3.5.2 Stress Relaxation

As explained in the literature review, silicone-rubber undergoes stress relaxation under a constant displacement. This relaxation of the material is an important consideration in this research, since the DIC measurements could not be automatically synchronised to force measurements from the UTM. Force measurements were taken at a period of constant displacement, which introduces variability due to stress relaxation of the material. An analysis of the maximum possible error in the force measurements (specifically due to stress relaxation at constant displacement) had to be included here to ensure that it was acceptable.

To quantify the variability of force at periods of constant displacement, the experimental protocol was repeated with longer periods of constant displacement (25 s instead of 2 s) at each displacement interval. Increments 3-7 (Figure 4.2) were considered in this analysis. For each period of constant displacement, the maximum deviation of force due to stress relaxation was studied. Table 3.6 shows the force variation over each increment of constant displacement as a percentage of the average force for each interval. Equation 3.1 shows how these values were calculated. The third column in Table 3.6 shows the time to constant force, which was defined as the time (from the start of the displacement increment) to the moment where the time derivative of force was between 0 and -0.001 N/s, which was seen as a negligible variation in force.

Table 3.6: Variation in Force Values for Different Intervals of Constant Displacement

Interval	Force variation [%]	Time to Constant Force [s]
3	2.80	3.45
4	2.54	4.62
5	2.78	6.03
6	2.77	10.27
7	2.76	11.22

$$ForceVariation(\%) = \frac{100 * (F_{max} - F_{min})}{F_{ave}} \tag{3.1}$$

In Equation 3.1, F_{max}, F_{min} and F_{ave} represent the initial, final and average force values for a displacement interval, respectively. The variation was averaged for six repetitions of the same test. The longer period of rest (25 s) was implemented to ensure that a long enough period of constant deformation was implemented for transient effects to die out.

Even though the time to constant force was consistently larger than the 2 s period of rest used in the loading procedure, the force variation over a displacement increment was consistently less than 3 %. The amount of variation in a period shorter than the time to constant force would be even smaller and the effect of stress relaxation was therefore considered negligibly small.

This method of loading the sample was not ideal, however a trade-off had to be made between the size of the load cell (and the measurement resolution) and the ability to capture measurements simultaneously. It was accepted that a maximum possible error in the force measurements of less than 3% was small enough for the method of loading to be seen as acceptable.

3.6 Validation of FEM Update Method Results

In order to validate the accuracy of the material model obtained from the FEM update method, a different test geometry had to be implemented. In this validation test, experimental results would be compared to the results of an FEA using the obtained material model. If the material model from the FEM update method is accurate, the FEA in which the model was implemented should give the same displacement results as an experiment using the new geometry.

In the case of this experiment larger samples were used such that samples could be gripped without causing significant stress concentrations in the area where

measurements are taken. The geometry of the validation sample is shown in Figure 3.5. Validation samples were loaded in tension and only the speckled area indicated in the figure was used for DIC.

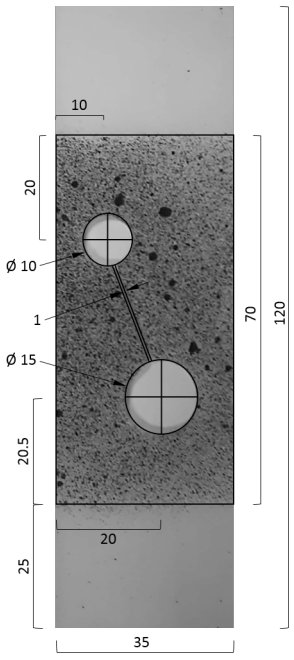

Figure 3.5: Validation Test Sample Geometry (Dimensions in mm)

This geometry was chosen, because it was expected to have a complicated strain field. The expected strain field was confirmed using an FEA as shown in Figure . It may be seen that the expected strain field would have areas of both compression and tension. The finite element model (FEM) for the validation test included the speckled part of the sample and an extra 5 mm at the top and bottom to replicate how the sample was clamped in reality. The FEM is shown in Figure 3.6 (A).

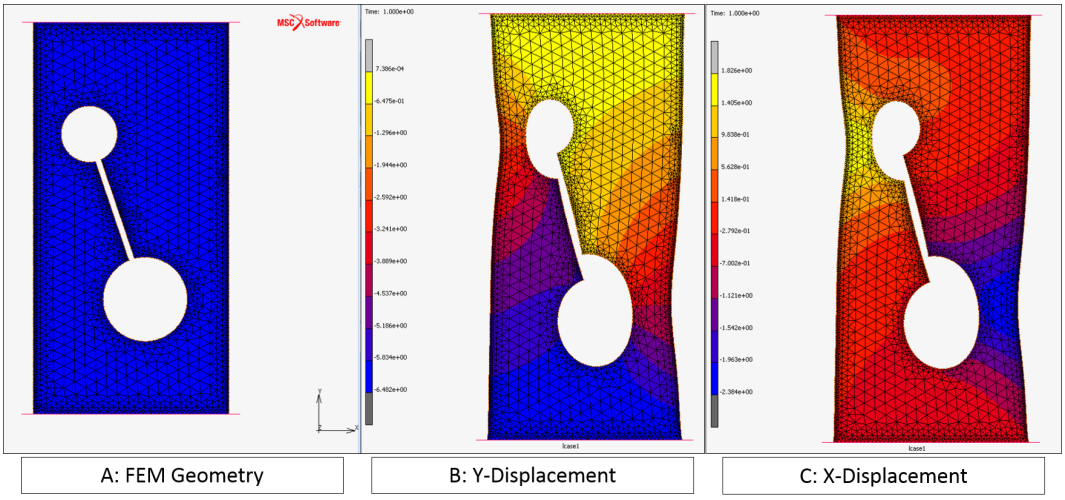

Figure 3.6: A: FEM Geometry, B: Y-displacements, C: X-displacements

3.6.1 Mesh Refinement Study

A mesh Refinement Study was performed for the proposed Finite Element Model in order to decide what the most appropriate mesh size would be for the simulation. When deciding on the best mesh size for a FE simulation two parameters need to be taken into consideration: model accuracy and simulation time. In general finer meshes lead to more accurate results, but longer simulations. However, the accuracy of the simulation will reach convergence at some point, leading to a small improvement in accuracy for a large gain in simulation time. The goal of a mesh refinement study is to ensure accuracy of the output while keeping the mesh as course as possible to avoid long simulation times.

In the case of this research the simulation time will have to be carefully considered, since the FEM update method will run the analysis multiple times. Figure 3.7 shows the results from the mesh refinement study in this research. In Table 3.7 the results of the mesh refinement study are summarised.

Table 3.7: Mesh Refinement Study

Elements	Maximum Y Displacement	Relative Convergence (%)	Wall Time [s]
500	-1.749545	NA	4
4000	-1.771392	1.2487	52
13500	-1.786678	0.6829	835
32000	-1.793856	0.4018	1784
62500	-1.798431	0.2550	6332

It may be seen that between a mesh with 13500 elements and one with 32000 elements the simulation time doubled, while the maximum observed displacement converged to within 0.5%. The final mesh was set up such that all elements had a length of 0.125 mm in all three directions, which resulted in 31280 elements and a wall time of 684 s. The maximum displacement for this mesh was -1.7943 mm.

Chapter 4

Experimental Method

The design for this project involved designing the physical experimental setup (Chapter 3) as well as the experimental protocol to be implemented before, after, and during testing with the aim of achieving accurate, reproducible results. This chapter describes the experimental- and data processing methods used to evaluate the design. The experimental method can be divided into four sections. First, there is a section on the preparations needed for experimentation, second, the protocol for the experiment is discussed. The third and fourth sections describe the methods used during post-processing and the inverse method, respectively.

4.1 Preparation

Preparation of both samples and the laboratory was needed before experimentation could proceed. Table 4.1 shows a list of the materials and equipment needed for the preparations described in the rest of this section.

4.1.1 Sample Preparation

Silicone-rubber samples were manufactured using a 3D printed plastic mould. The mould could produce nine 10 x 10 x 2.5 mm samples per batch and the design is available in Appendix B.0.1.

The mould was 3D printed from ABS (acrylonitrile butadiene styrene) plastic, which is dissolvable in acetone. To smooth out the ridges inherent in a 3D printed part, the mould was placed in a sealed container with acetone drenched cotton wool. As the acetone evaporated from the cotton wool, the outer layer of the mould dissolved, causing the surface to become smooth. As a result, the mould could produce samples with a smooth surface finish for use in DIC.

A two-part silicone-rubber was used to prepare samples a day in advance of testing. The data sheet for the material is available in Appendix C. To keep

Table 4.1: List of Materials and Equipment

Sample Preparation		**Laboratory Setup**	
Materials	**Equipment**	**Materials**	**Equipment**
Acetone	Mould	White Paper	Universal Testing Machine
Ecoflex 00-30	Cotton Wool	Sellotape	5 N Load Cell
Powder Pigment	Plastic Container		Measuring Tape
Baby Powder	3 Large Syringes		Ruler
	Scale		Cameras
	Vacuum Chamber		Tripod
	Vacuum Pump		LED Lights
	Curing Oven		DIC controller
	Stopwatch		Trigger Button
	Beaker		UTM attachments
	Stirring Rod		Calibration Plate

the material properties of the samples as consistent as possible, the following method was used to produce each batch of samples.

1. Heat curing oven to 70°C.
2. Mix together equal parts (by weight) of the two-part Smooth-On Ecoflex 00-30 silicone rubber.
3. Deposit the mixture into the mould using a syringe to prevent overflow.
4. Place the filled mould in a vacuum chamber for ten minutes to degas.
5. Check the mould for residual air bubbles and the fill level after degassing and repeat steps (3) and (4) if necessary.
6. Cure samples for 20 minutes in the preheated curing oven.
7. De-mould samples, leave them to cool and trim if necessary.

Step (4) was crucial to remove any bubbles trapped in the mixture. A sample containing bubbles cannot be treated as a homogeneous material and the material behaviour will be unpredictable (Meunier *et al.*, 2008). The process of degassing is recommended by the silicone rubber supplier.

The process of degassing could cause the fill level in the mould to drop slightly, therefore step (5) was implemented to ensure that sample height was reproducible. Any excess mixture was scraped off the top so that the meniscus, which forms naturally, was as small as possible. If a refill was necessary, the sample had to be degassed a second time. This extra step would not influence the material properties of the cured samples since the material has a long curing time at room temperature (Appendix C).

To cure the silicone-rubber mixture, the filled and degassed mould was placed in a preheated oven at 70 °C (Step (6)). This offered better control over the curing process because samples were all cured at the same temperature as opposed to curing at room temperature, which could fluctuate from day to day. The mould material could withstand the curing temperature without deforming.

4.1.2 Laboratory Setup

The laboratory setup involved the configuration of the universal testing machine (UTM) and placing and setting up the DIC system. Additionally, the air conditioning system was set to 18°C to maintain a constant temperature between different days of testing.

4.1.2.1 Universal Testing Machine (UTM)

The UTM (Instron 3345) was used to apply a force to the test specimen. A 50 N load cell was used as discussed in the design section. Figure 4.1 shows the different attachments of the UTM machine as referred to throughout the chapter.

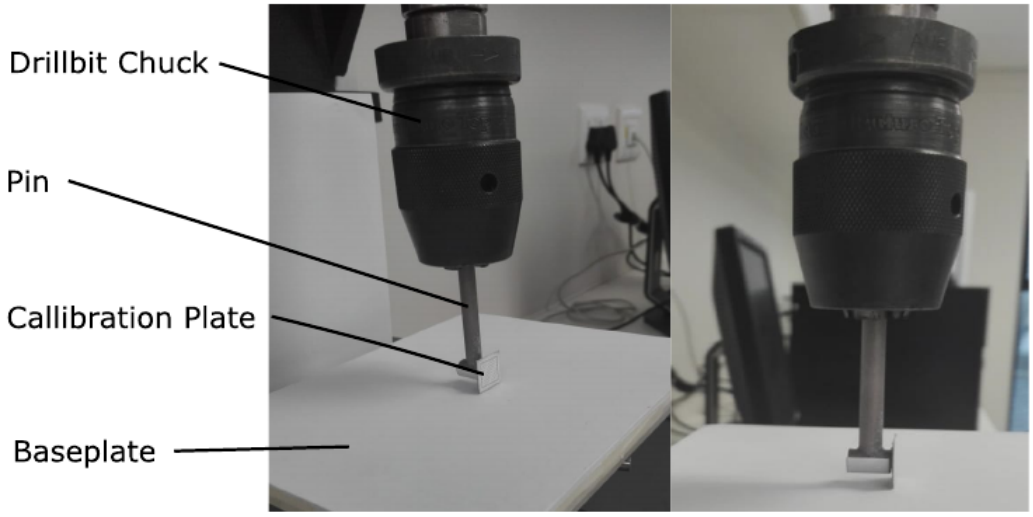

Figure 4.1: UTM Attachments

A white baseplate was used to avoid overexposure due to reflective metal parts. The UTM (specifications shown in Table 2.2) was set up, as shown, with the necessary attachments, including the 50 N load cell, and the sample was loaded in compression. Since samples were thin (2.5 mm high), there was a risk of load cell failure. If the UTM extended too much, the sample could deform to

such an extent that the pin is effectively in contact with the baseplate, which would cause the compressive force to be higher than the load cell rating.

The UTM has a built-in safety mechanism to avoid overloading of the equipment. To set up the safety mechanism, the crosshead must be moved until the pin is just above the baseplate. Then, the safety knob has to be screwed into place. This mechanism sets a mechanical limit for the crosshead displacement, which automatically stops displacement before the bit hits the baseplate. The pin was designed specifically for this project. The dimensions of the pin are available in Appendix B.0.2. It is attached to the UTM using a drill bit chuck. The last step in setting up the UTM was defining the control protocol for the displacement of the crosshead.

The UTM was programmed, using Instron® Bluehill 3 software, to implement displacement control of the crosshead. The software has a graphical user interface, which uses blocks to create a displacement protocol for the crosshead of the machine. Since the chosen UTM could not connect to the DIC system to make simultaneous measurements, quasistatic displacement steps were used. This way, DIC measurements could be taken manually at each displacement increment, as a way of synchronising strain and load measurements. Even though this method is not ideal, it was a trade-off that had to be made between the resolution and minimum load cell size of the machine and the synchronisation of the results. The amount of error caused by this design choice is discussed in chapter 5. The protocol was programmed to increment the displacement between 0 mm and 1.8 mm in increments of 0.2 mm at a time. Figure 4.2 shows the displacement versus time graph implemented for crosshead displacement control.

Samples were preconditioned, by cycling between the minimum and maximum displacement six times, to eliminate any unrepeatable effects due to strain hardening of the sample material. For every batch of samples, one specimen was cyclically compressed ten times to study how the maximum force converged with each compression cycle.

4.1.2.2 Digital Image Correlation

As discussed in Chapter 3, the DIC system was set up by mounting all the components on a tripod (Figure 2.9, P. 24). It was set up such that the camera was at a height where the sample could be viewed directly from the front through the captured images. A test sample was placed in position on the UTM platform so that that the DIC hardware and software could be configured and calibrated.

The first step in adjusting the DIC system was to make sure that the sample was properly in focus by adjusting the positions of the cameras and the settings of the lenses. This was particularly important since the image focus would

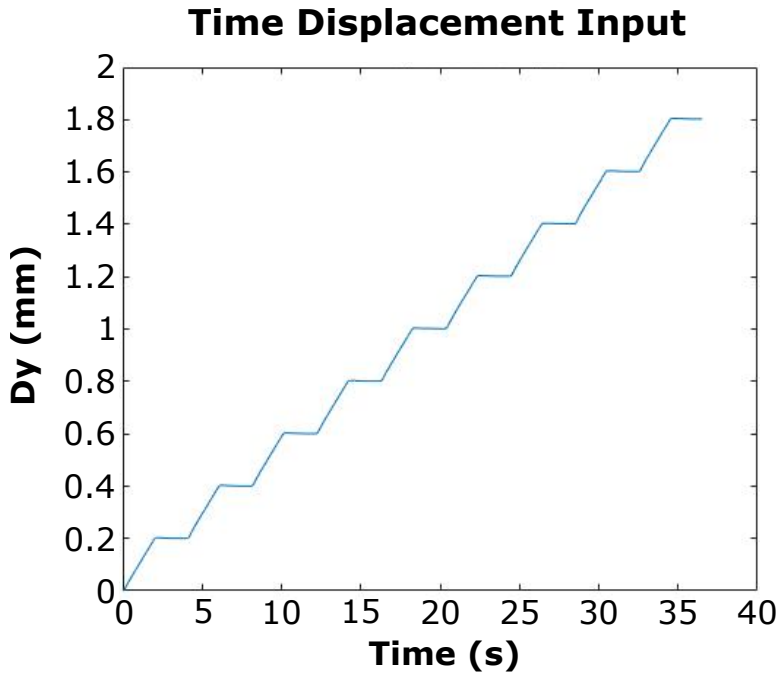

Figure 4.2: Displacement Control

determine whether the data could be captured. The limiting factor for this sample size (10 x 10 x 2.5 mm) was whether the depth of field of the photo would be large enough for the samples to be in focus, even when they were fully deformed, as discussed in chapter 2.

In Chapter 3, it was shown that the best depth of field (DOF), with the smallest area of focus, occurred when the aperture was at its smallest. For this reason, the lens was first set to the smallest possible aperture before the focal length was fine-tuned in order to perfect the focus. The larger the aperture of the lens, the smaller the DOF and the larger the possibility that sample deformation could cause the surface of the sample to go out of focus during testing. Once the focus was fine-tuned, the next step was to check the lighting and the contrast of the cameras.

The lighting was set up to ensure that there were neither areas of over- nor underexposure. This had to be true even when the sample was at maximum deformation otherwise, the DIC algorithm would not have been able to identify features on the surface of the sample. The lighting and contrast of the images could be adjusted in various ways.

The lighting was adjusted by moving the LED lights around, adjusting the brightness of the flash, or covering the LED lights with a material that scatters the light. Although the contrast and exposure were also influenced by the aperture of the lens, the adjustments to the lighting were the final step in

ensuring proper contrast, since the aperture had to be kept as small as possible.

For the successful use of DIC, the system must be calibrated. The calibration of a DIC system involves calculating the relative positions of the cameras to the sample (angles, object distance, etc.) and to each other in order for the software to calculate displacements on the surface of the sample (as discussed in Section 2.6).

Calibration plates were manufactured as discussed in Section 2.6.4 (P. 17). The final geometry of the calibration plate was shown in Figure 2.7. DaVis DIC (LaVision, GmbH) software was used to create a printable pdf of the plate. These were then printed, at the correct scale, and attached to a cardboard backing for use during experimentation. Lastly, the surfaces of samples were speckled to provide unique features which the DIC software could use to track displacements.

Typically, samples are speckled using an airbrush right before experimentation starts. It is crucial to ensure that the paint is still a little damp during experimentation to avoid cracking of the paint during deformation. This method of speckling the sample did not work well for the specific application. The paint did not stick to the surface of the sample well and it tended to dry before the experiment could be completed because the sample surface area was so small. It was therefore decided to apply the pattern using a black pigment powder instead.

The powder stuck to the surface of the sample because the sample material naturally had a tacky surface finish and the particles were small enough to form enough features within each subset of 30 pixels, which was the minimum allowable subset size.

During preliminary tests, it was found that the surface of the samples was matte before deformation, but after deformation, the surface became more reflective. This posed a problem because shiny surfaces reflect light and cause the associated images to have spots of overexposure. To prevent this from happening the surface of each sample was dipped in talcum powder after the speckle pattern was applied.

An advantage of applying the speckle pattern in this manner was that samples could be speckled well in advance of the experiment since there was no paint which could dry before the experiment was completed.

4.2 Experimental Protocol

The following protocol was repeated for each sample. It ensured the success of the DIC process and that the correlation between measurements from the load cell and the DIC system was satisfactory.

Step 1: During experiments, DIC hardware was kept stable using a tripod. Everything was first set up correctly, whereafter the whole setup was locked in place.

Step 2: The sample was placed on the UTM baseplate. The correct location of the sample was marked on the baseplate to ensure the sample is properly aligned to the cameras. A final check was done to ensure that the focus, lighting, and exposure were acceptable. If needed, fine adjustments to these parameters were made before DIC calibration could start.

Step 3: The calibration plate was used to calibrate the DIC system. The plate was attached to the front of the pin since it could not be attached to the sample. For calibration using the method described in Section 4.1.2.2, eight images of the calibration plate, in different orientations, were taken. DIC software then identified the markers on the plate, and once it was verified (by the researcher) that the software identified the markers correctly (in each image), the calibration step was completed by the software. Calibrations were not transferred between individual tests.

Step 4: A manual trigger was used to initiate DIC measurements. These measurements were synchronised to the load measurements by pressing the trigger at every displacement increment. The displacement of the UTM crosshead was monitored, using the live displacement graph on the Bluehill user interface, to make sure that measurements were triggered at the correct time.

Step 5: After testing, an area of interest was defined in the DIC software, in order for it to calculate the raw displacement data. The area of interest was chosen such that the edges of the sample and the outline of the area of focus matched as far as possible. Then, seeding points (for DIC elements) were chosen to start the subset identification stage. The desired size and spacing of the DIC elements were specified to ensure the distribution of data points on the surface of the sample would be satisfactory as discussed in Chapter 2.

Step 6: The maximum expected amount of deformation (1.8 mm) was set and a quick test was run to ensure that the processing quality was satisfactory before running the final DIC calculation.

As explained in Chapter 3, data obtained from the experimental process included the deformation of the sample in three dimensions (.dat file from DIC) and the corresponding load, displacement and time data from the UTM machine. Displacement data was extracted from the DIC results as a series of displacement vectors, one for each DIC element.

After the data was processed (post-processing discussed in Section 4.3), the results from the inverse FEM update method (discussed in Section 4.4) had to be validated to ensure that the material model obtained was accurate.

Validation of the results involved using the same protocol, but in a different test geometry.

4.3 Post Processing

Post-processing of the raw experimental data included an analysis of the quality of the data, eliminating 'bad' data from the dataset, and fitting surfaces to the displacement fields obtained in the DIC experimentation process. A statistical analysis of the entire dataset was performed, but it will only be discussed in Chapter 5. This section focuses on the process involved in calculating the material model itself.

4.3.1 Data Extraction

Raw data from the DIC experiment was exported as a Techphlot (.dat) file. This file contained columns for the initial x-, y-, and z-positions of the DIC elements as well as columns for the x-, y-, and z-displacements at each of these initial positions. This data was imported into MATLAB R2017b (MathWorks®) for further processing.

First, data had to be masked. Even with a successful DIC analysis, there will be some data points that disappear when they cannot be 'seen' by the cameras, due to the deformation of the sample. DIC software also supplies raw data for the entire image instead of just the area where the sample is found. Data points outside the area of interest and data points which disappear from the camera view are assigned a displacement value of zero in all directions. These zeros are not an accurate representation of how the sample deforms in real life. Data points outside the area of interest were masked out using a rectangular masking function. Data points which disappeared from the camera view were given not-a-number (NaN in Matlab) displacement values so they could be omitted during surface fitting and error calculations.

Next, the data was transformed such that the initial positions would match the corresponding positions in the FEM model. The displacement field was analysed to determine the true placement of the samples. The location in the x-direction where the largest average displacement (in the y- and z-directions) was found, was assumed to be the x-coordinate of the point of contact with the pin. A basic translation of the initial position was performed such that the x-coordinate would reflect the location of the pin in the FEM model. The first location in the y-direction where all displacement values were zero was assumed to be the zero position in the y-direction. These translations help to

correlate the position information to the FEM model and have no impact on the displacement results.

Further post-processing of the data consisted of two steps: data disqualification and curve fitting. Data disqualification involved analysing each individual DIC experiment's results since some variability will exist as a result of small geometric differences in the placement of the sample. Data disqualification ensured that the data used for the inverse method was of an acceptable quality. Surface fitting, on the other hand, involved applying fitted surfaces to the experimental displacement data. These surface fits were used to map displacement data between DIC elements (from the experimental results) and the FEM nodes for the inverse FEM update method.

4.3.2 Data Disqualification

When analysing large quantities of raw data, it is important to ensure that the data is of a good quality. Data of a poor quality may be the result of factors including equipment failure and human error. For final results from an experimental process to be of a good quality, the raw data must be of a good quality as well. Flawed data cannot be used to generate accurate results.

Since the experiments in this research were conducted at a small scale of observation (10 mm), the quality of the data is very important. The quality of raw data can be determined from either a statistical analysis or by identifying specific criteria for when the results from an experiment may be considered invalid for the purpose of the experiment.

A statistical analysis of the data provides insight into how the value of an individual measurement compares to the average value for all measurements, but not into why the variation occurred. The identification of poor data using statistical methods relies on the identification of outliers (values that differ greatly from the average result). The challenge with this method is ensuring that the identified outliers are in fact measurements which do not reflect an accurate raw result.

The second option, where physical criteria are used to eliminate data of a poor quality, is based on an insight into the requirements of the experimental process. It does not consider the value of the raw result, but the variation in experimental variables. It is not always possible to apply this method since it might not be possible to determine the values of all experimental variables, but in the case of this research, the DIC results provided a physical measure by which data could be disqualified.

The experimental method in this research used a compression test to determine material properties. In this way, the need for clamping the samples was eliminated, but the samples had to be placed, with reasonable accuracy, in

a specific orientation on the baseplate of the UTM. It was known that there would be some variation in the placement of samples, which was done by hand. Although precautions were taken to ensure that the placement of samples was as accurate as possible, there was still some variation between experiments. Fortunately, it was possible to use the DIC output to determine by how much the placement of a sample deviated from the ideal.

Angular deviation and X-shift were identified as the two variables which could determine whether or not the placement of each sample was acceptable. These variables were quantified in terms of the placement of the samples in reality (determined from DIC results) in comparison to the ideal placement of the samples. Figure 4.3 illustrates how these values were calculated.

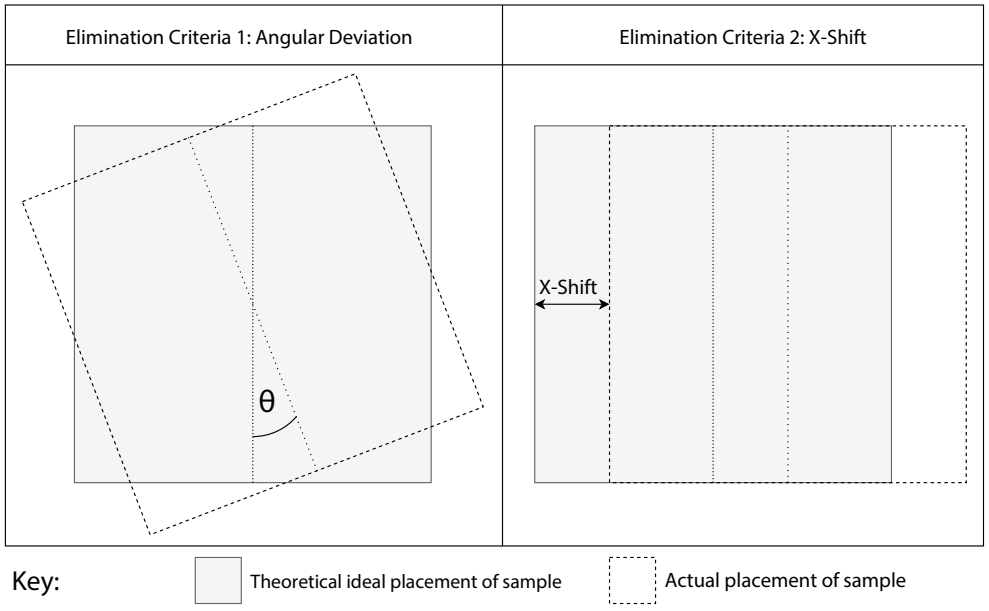

Figure 4.3: Definition of Disqualification Variables (Top View of Sample)

The angular deviation (further referred to as deviation) was defined as the angle by which the axis of a sample varied from the ideal. According to the experimental design, the speckled surface of the sample should be perpendicular to the centre line between the two cameras (Refer to Figure 2.5). The deviation was calculated by calculating the angle of this surface, with regards to the ideal, using the z-position coordinates from DIC. The maximum allowable angular deviation was defined as 1°, which would correspond to less than 0.1 mm of deviation in the z-direction (less than 1% of sample size). This was seen as a safe threshold for deviation from the correct orientation of the sample on the baseplate.

The X-shift was defined as the amount by which the sample was shifted in the direction parallel to the surface. This criterion was defined as the distance

between the centre plane of the pin and the centre plane of the sample. The maximum allowable X-shift was defined as 0.25 mm.

If the placement of a sample did not comply with either one of these criteria, the test was seen as a failure and the data from that test was excluded from further analysis to ensure that variability due to experimental errors were eliminated as far as possible.

4.3.3 Surface Fitting

After data disqualification, only a few sets of data remained. These datasets were obtained from individual tests where the samples were placed correctly in the experimental setup, which meant they would have a good correlation to the FEM in terms of geometry. Before surface fits could be applied, the remaining sets of data had to be averaged to obtain a single set of force-displacement values. Only the averaged data was used in the inverse FEM update method to determine the appropriate material model for the behaviour of the material.

For data from the DIC process to be compared to data from the FEM simulation, it was necessary to map data points from one output to the other. In other words, to properly compare results from the simulation to results from experimentation, it was necessary to know the same information (displacement values) about the same point in physical space. A surface fit was applied to one data set to find the corresponding values for displacements at a different initial position in the other dataset. It is important to note that the displacement data in a 3D simulation consists of displacements in three directions. In other words, every set of force-displacement data contains one value for applied force and three respective values for displacement in the x-, y-, and z-directions. The displacement data for each direction was unique and three curve fits were generated for each displacement increment. Please refer to Section 2.8 for a more detailed description of the mapping procedure.

Surface fits could be applied to either the DIC or the FEM outputs. Since the data from the DIC experiments was already determined, and could not change during the process of optimization, it was decided to apply a surface fit to the experimental data. Mapping from the FEM data would require fitting a surface to the FEM output for every iteration of the optimizer, which could increase the computational cost. In addition, it would be difficult to check the quality of surface fits during the optimization process. Fitting to DIC data therefore saved computational time and enabled the researcher to control the quality of the applied fit before the optimization process started.

For this research, cubic interpolation surface fits were used in the data mapping procedure. Multiple options were investigated in this regard, but interpolation provided the best outcome. Surface fits were functions of the initial positions (x and y) for each node in the DIC analysis of the deforming surface. Initial

positions in x and y of the FEM analysis could therefore be used to calculate corresponding experimental values for each FEM node. These surface fits served as mapping functions between the experimental results and the output from the finite element model.

For the surface-fitting process, any locations where the DIC software was unable to identify subsets on the surface of the sample (as a result of compressive deformation) were ignored. These locations on the surface of the sample were also ignored during the calculation of the root mean square error during optimization.

4.4 FEM Update Method

The inverse FEM update method uses an optimization algorithm to iteratively solve a material model from force and displacement data. The optimization process was described in Section 2.8 and a flow chart of the process is available in Figure 2.8 (P. 19). This section will discuss how the inverse FEM update method was implemented using a FEM model and how the objective function was calculated. VisualDOC 7.2 (Vanderplaats RD. Inc.) optimization software was used for the optimization process.

4.4.1 Finite Element Model

The inverse FEM update method consists of a finite element simulation within an optimization loop as explained in Section 2.8. The FEM model was identical to the sample, in geometry and loading or boundary conditions, and any simplifications had to be well motivated. As explained in Section 2.8, this method of post-processing is an implicit method of solving for the material model of a material using force and displacement data. It is a black box method, used to determine a material model if a sample has a complex deformation field. In such cases, the mathematical solution for a material model would be tedious or even impossible to solve explicitly. The optimization loop was an iterative alternative method of determining the material model.

Iterative optimization methods like these present the drawback that the material is modelled without an understanding of why it behaves in a certain way. The solution is not obtained through an understanding of the material's behaviour, but by describing the measured behaviour of the material as accurately as possible. This means that, even though the mechanics of the material behaviour are not fully understood, the material behaviour can be predicted in a useful way.

The finite element model for this experimental setup was simple. It was a hexagonal sample of material being compressed by a pin. For this project, it was decided to use non-linear FEM software (MSC Software, Marc Mentat

2017.1.0). This kind of software was required since the sample would be made out of non-linear material, which would be in contact with a flat surface at the bottom and a pin applying pressure from above (Figure 4.4). Both contact and non-linear materials require a non-linear solver. The chosen software was MSC Marc and Mentat since there was a lot of expertise available and it is a well established non-linear solver.

The FEM model used a three parameter Mooney-Rivlin material model to describe the material behaviour. This model is defined by three constants ($C10$, $C01$ and $C11$). Scaled values of the material constants served as the optimizer variables in the inverse FEM update method.

To save computational time and to make the simulation more stable, only a quarter of the sample was included in the model. Instead of modelling the whole sample and applying boundary conditions to its surface, the boundary conditions were implemented by symmetry conditions. When using symmetry conditions, rigid body nodes are eliminated, since these boundary conditions are applied to a whole surface instead of a single node. Boundary conditions, which ensure the sample does not move around during the simulation, do not transfer well between meshes when remeshing is applied. This problem is avoided using symmetry. In addition, it was found that remeshing was not necessary for compressive strains of 20-55 %, which was the range implemented in the model. The model geometry is shown in Figure 4.4.

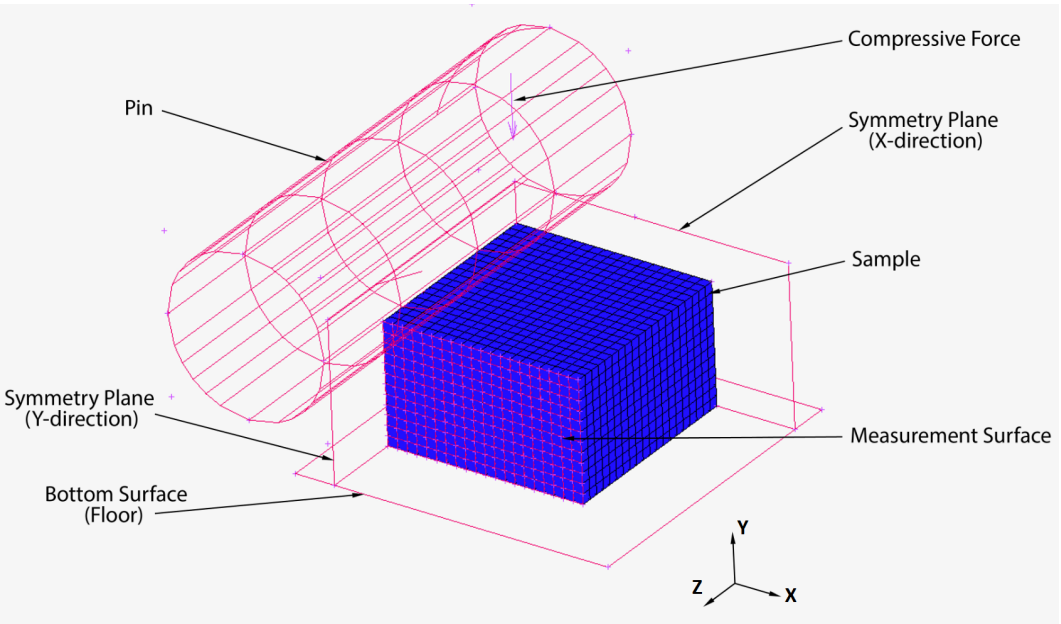

Figure 4.4: Finite Element Model

The sample is in contact with geometric surfaces at the bottom (bottom surface) and the top (pin). The contact between a deformable body (a meshed

solid that can deform) and a geometric surface (cannot deform at all) can be classified as either glued or touching contact. Glued contact connects the surfaces to each other in such a way that the nodes in contact with the floor surface cannot move. It is similar to applying zero displacement constraints on all the nodes in contact with the surface. Implementing a glued contact condition is more stable than implementing a constraint type boundary condition.

Touching contact, on the other hand, does not limit the displacement of nodes in all directions. Instead, the deformable body is only constrained in the direction perpendicular to the geometric surface in such a way that nodes in contact with the geometric surface cannot move through it with the application of force. This type of contact does not limit the sample from lifting off the contact surface and allows more freedom for the deformation of samples. The touching contact condition is more difficult to implement than glued contact.

Since touching contact does not constrain the movement of the sample, extra boundary conditions could be necessary to ensure convergence. In the case of this research, however, this problem would be avoided by the use of symmetry planes as the symmetry condition automatically enforces zero displacement boundary conditions in directions perpendicular to the symmetry plane.

Preliminary tests showed that the surface of the silicone material was sticky. The effect was that the sample stuck to the surfaces of the testing rig (baseplate and pin, see Figure 4.1) and a glued contact condition was assumed to represent this behaviour.

The final FEM model was identical to the actual sample in terms of geometry, which was achieved by finding the actual dimensions using the experimental DIC results. Other parameters, like the mesh size, are available in Table 4.2. Results from each finite element simulation are the displacements in three directions for each node on the measurement surface at each increment which falls between deformations of 20-55 % compressive strain.

Table 4.2: Finite Element Model Summary

Parameter	**Description**
Element Type	First Order Hexagonal
Number of Elements	31280
Number of Nodes	34441
Material Model	Mooney-Rivlin
Number of Material Parameters	3
Simulation Length	1 second
Type of Control	Force
Residual Error Convergence	10^{-6}
Solver	Pardiso Sparse Solver

4.4.2 Objective Function

The objective function was a root mean square error (RMSE) value between the experimental results and the FEM simulation. As discussed before, surface fits (mapping functions) were used to relate the initial positions of FEM nodes to the experimental displacement data from DIC experiments.

The first step in the data mapping process was to find nodes in the DIC data that surround the FE nodes. These DIC nodes were referred to as the neighbours of the FEM node. Each FE node had four neighbours, whose coordinates fall just below and just above the coordinates of the FE node in both in-plane directions. Next, each of the neighbours for each FEM node was evaluated for the displacements it had undergone. If the node was surrounded by two or more false zeros (points where the DIC software could not extract displacement data), it was not used in the evaluation of the FEM's accuracy.

The equivalent experimental displacement of each node was evaluated using a linear interpolation function between the three or more DIC neighbours. A linear fit was chosen, since it produces an almost identical fit to the cubic interpolation, even though it is of a lower order. Initially, it was attempted to fit a polynomial function to the entire dataset from the DIC analysis, but better results were achieved using interpolation.

The equivalent experimental displacement was essentially the mapped values of the experimentally measured displacements. These displacement values were used to calculate an RMSE value between the displacement observed in reality and the displacement calculated by the FE simulation. The equation used to calculate this error is available in Section 2.8 (Equations 2.8 to 2.11). The RMSE served as the objective function for the inverse FEM update method.

For the optimization process, the optimizer variables ($SC10$, $SC01$, $SC11$) were scaled values of the three parameters of the Mooney-Rivlin material model ($C10$, $C01$, $C11$). The lower limit for the values of these variables was zero, as negative values could cause the FE analysis to become unstable.

The convergence of the finite element analysis (FEA) is indicated in the Marc output file as an exit number. An exit number of 3004 indicates that the model converged successfully. The success of the FEA had to be checked before the objective function was calculated, or else the FEM output data would be incomplete. An exit code was implemented in the optimization process to avoid the use of incorrect or incomplete data in the calculation of the objective function. The exit code was assigned a value of -1 if the FEM simulation was successful and a value of 1 if the simulation was not successful. The exit code was included in the optimizer as a constraint, where the upper allowable value was zero. This would force the optimizer to iterate different material models until the FEA converged.

The optimizer aimed to minimize the least squares error by iterating different values for the material parameters in the FEM. A least squares error with a value of zero would indicate that the results from the finite element simulation matched the experimental results perfectly. At the point in the optimization process where the RMSE is at a minimum, the material model should (theoretically) be the best model to describe the material behaviour.

The next section will discuss the results obtained from this optimization process.

4.4.3 Optimizer Parameters

The Optimizer used in this research used the Modified Method of Feasible Direction as its search method. It employed a central differencing scheme with relative and absolute finite difference step sizes of 0.1 and 0.1 respectively.

The maximum number of iterations was set to 15 and six iterations were seen as convergence of the model.The relative objective convergence had a value of 1^{-4} and the absolute relative convergence was set to 1^{-6}.

Chapter 5

Results and Discussion

When analysing the quality of experimental data or experimental results, precision and accuracy are two important factors to take into account. Precision is an indication of the repeatability of the result. If results from an experiment are precise, the results from consecutive tests should be very similar. Precision, however, does not indicate whether the result is correct. Accuracy indicates if results are realistic. For an experiment to be successful, results have to be both accurate and precise. In this chapter, both the raw and processed results are evaluated in terms of these two factors by discussing the statistical analysis of the raw data, factors which contribute to variability, results from optimization, and the validation of results.

5.1 Statistical Analysis

The statistical analysis in this research gives an indication of the variability in the results. For this analysis, individual data points are analysed in terms of how they relate to an average of the whole data set instead of how they correlate with the real or ideal value. The statistical analysis does not give an indication of whether the results are accurate since no benchmark value was known before tests were conducted.

As discussed in Chapter 4, samples were produced in batches and one sample from each batch was cyclically loaded, to study the convergence of force values at maximum compression (1.8 mm crosshead displacement). Figure 5.1 shows how the values converged. Although force values varied between samples, the results of each sample consistently converged after 5-6 compression cycles. It was then decided that samples should undergo 6 preconditioning cycles before the experimental measurements would be taken. This would ensure that the force at maximum compression for each individual sample would be constant.

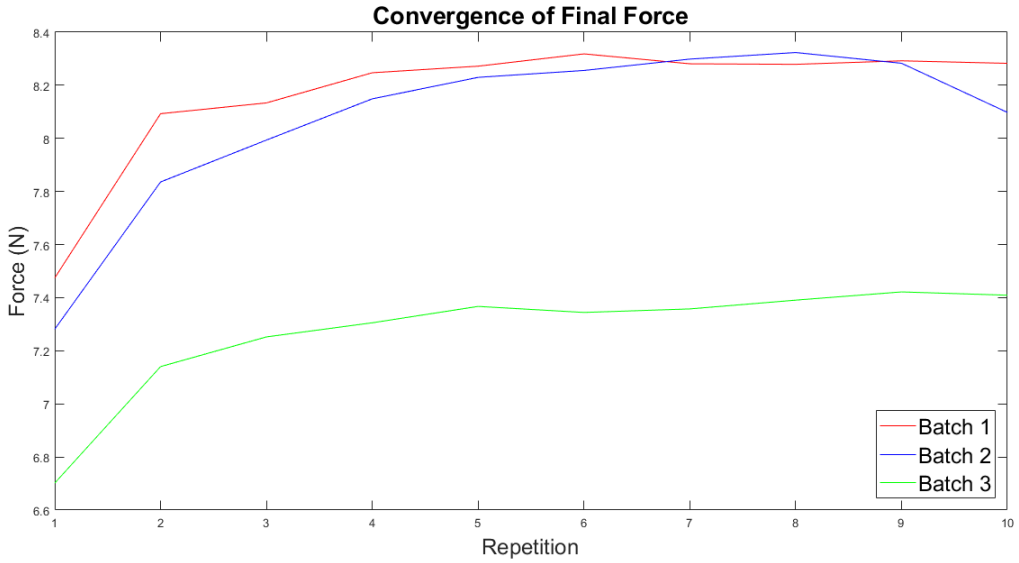

Figure 5.1: Convergence of Experimental Force Results

A total of 24 samples were tested. Results from one sample were discarded on account of human error. The remaining 23 samples were considered in this statistical analysis. Samples were compressed beyond the compression percentage limit which would be considered in the optimization process. Only compression values of up to 55 % (1.4 mm) were considered in the optimization, but samples were compressed up to 65.4 % (1.8 mm). Figure 5.2 and Figure 5.3, respectively, show the displacement versus time and force versus time results for all samples.

This statistical analysis procedure included calculating the average, variance, and the standard deviation of force and displacement data at each displacement increment. The displacement data gives an indication of the variability in the control of the UTM machine, which was the independent variable for these tests. The force data was the dependent variable. Figures 5.2 and 5.3 show that there was variability in the output force measurements, even though the input displacements showed little variation.

The mean and standard deviation of force for each displacement interval provides a better estimation of the specificity of the data since it quantifies the average amount by which each data point deviates from the mean value. These values can be plotted as a box-and-whisker plot as shown in Figure 5.4.

The first two displacement increments (Figure 5.4, Subplot 2) showed some variability, but these were below 20 % compression and were not considered in the optimization process. For increments I3-I9, the displacement data was extremely repeatable. Since the displacement is the independent variable for these experiments, it is important that it is repeatable. If the displacement

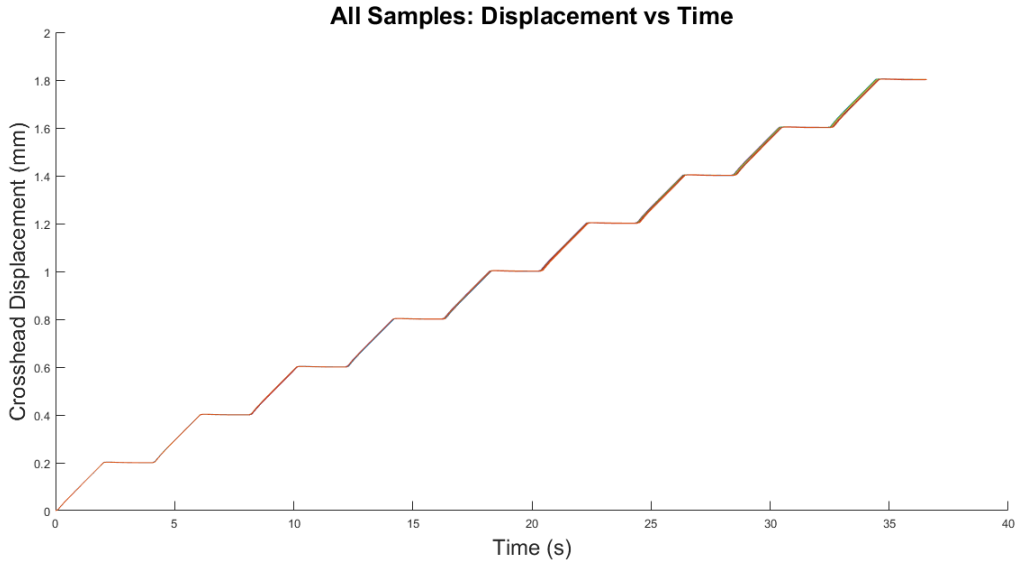

Figure 5.2: Displacement versus Time Data for All Samples

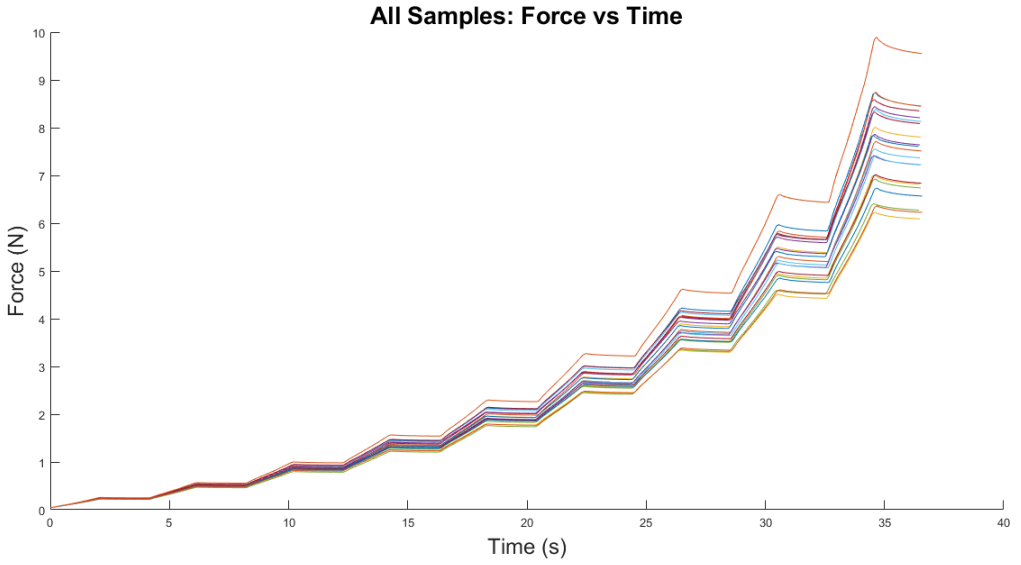

Figure 5.3: Force versus Time Data for All Samples

data was not repeatable, the experimental inputs would not be consistent between tests. The amount of variability in the displacement data for these tests may be seen as negligible for 20-55 % compression (I3-I7), which was the range used in the optimization process. Even though the input of the experiment was considered precise, the force data shows a significant amount of variability.

The size of the standard deviation of the force data generally increased with

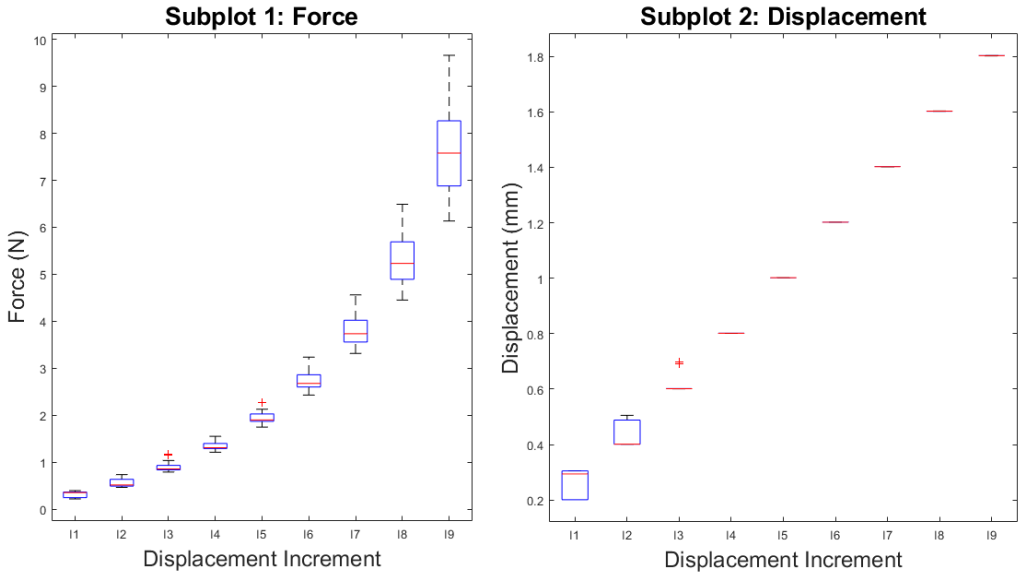

Figure 5.4: Box-and-whisker Plots of Force and Displacement Data

an increase in the amount of crosshead displacement. On the other hand, it is important to note that only increments I3-I7 fall within the range of compression percentages to be considered in the optimization process. Table 5.1 shows the values of the standard deviation for these increments as percentages of the average force at each displacement increment.

Table 5.1: Relative Size of Standard Deviation of Force Values for Increments 3-7

Increment	Average (N)	Standard Deviation (N)	Relative Size of Deviation (%)
3	0.8996	0.1020	11.34
4	1.3467	0.0910	6.76
5	1.9569	0.1439	7.35
6	2.7509	0.2215	8.05
7	3.8180	0.3432	8.99

The standard deviation for increments 3-7 was between 6.76 % and 11.34 % even though the displacement input was consistent throughout. The variability in the force data was likely caused by various factors, including human error, variability in the material properties, and noise in the force measurements from the UTM (0.25 N). The maximum force observed was < 10 N across the board (Figure 5.3), therefore the experimental method was very sensitive to measurement noise. Although the load cell with the smallest amount of noise was chosen, the noise in the signal was equivalent to 6.6 % of the average measured force at 1.4 mm compression (3.818 N), which could have contributed to the variability in force measurements.

Since the displacement data is very repeatable it was possible to plot the force against displacement data. Figure 5.5 shows the raw data, the mean and the bounds of the first and second standard deviations of the force versus displacement data for all displacement increments. Figure 5.5 confirms the force data shows a significant amount of deviation.

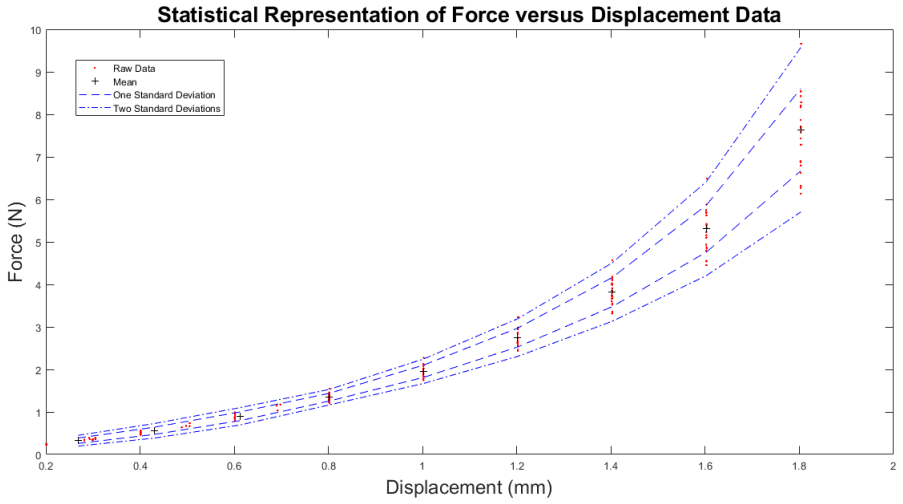

Figure 5.5: Force Versus Displacement Data for All Tests (Including Statistical Averages and Standard Deviations)

5.2 Disqualification of Data Due to Experimental Error

As discussed in Section 4.3.2, tests where samples were placed incorrectly were disqualified from further analysis.

Table 5.2 shows a summary of the number of tests where the placement of samples was not acceptable. Ten samples complied to the criteria.

Table 5.2: Number of Samples Eligible for Post-processing

Criteria	Number of Samples
Total	23
Eliminated	13
Fails on Deviation	13
Fails on X-Shift	6
Remaining	10

The displacement fields from the 10 remaining samples were averaged to produce the displacement field against which the FEM output would be benchmarked in the inverse FEM update method.

5.3 Surface Fits for Optimization

Surface fits (quadratic interpolation) were applied to the resulting displacement field to enable data mapping between the experimental and FEM results. Figures 5.6, 5.7 and 5.8 show the surface fits generated from the experimental data.

In the figures, the experimental data is represented as blue circles, with the fitted surfaces plotted continuously. Cubic interpolation fits were applied to the data using Matlab, which means that the correlation coefficient for these fits are 1. As explained in Chapter 4, locations where DIC data was incomplete were included in neither the surface fitting process nor the calculation of the root mean square error, therefore the surface fits shown do not extend to the whole range of experimental data in the figures. These surface fits were used to map data between the FEA and experimental results as explained in 4. Incomplete data was excluded from the mapping process, to avoid optimizing the material method to unacceptable experimental values.

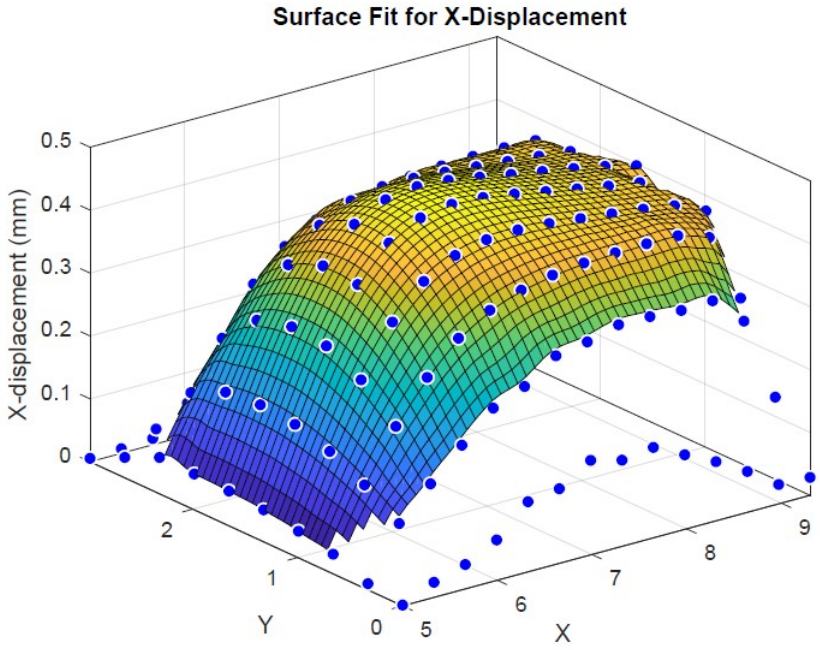

Figure 5.6: Displacement in X-direction

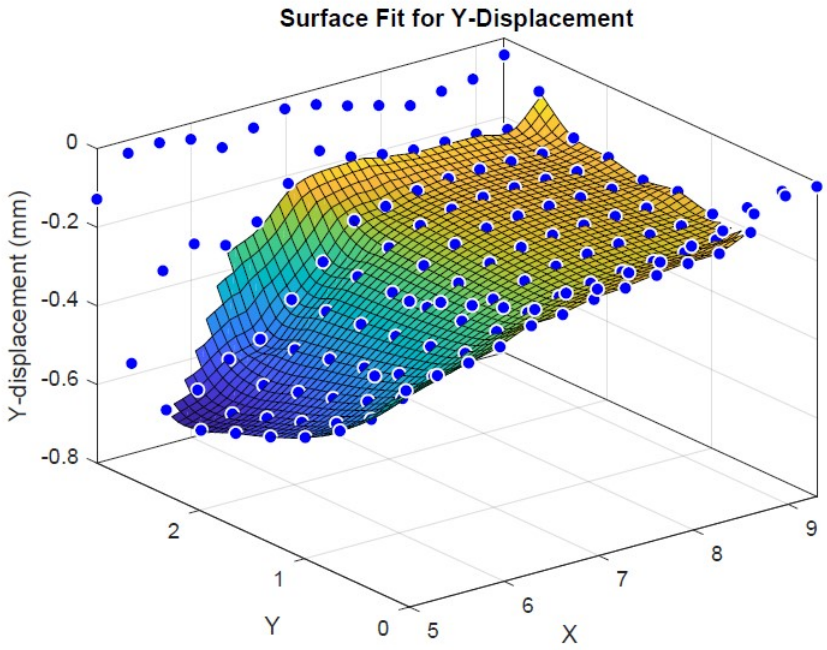

Figure 5.7: Displacement in Y-direction

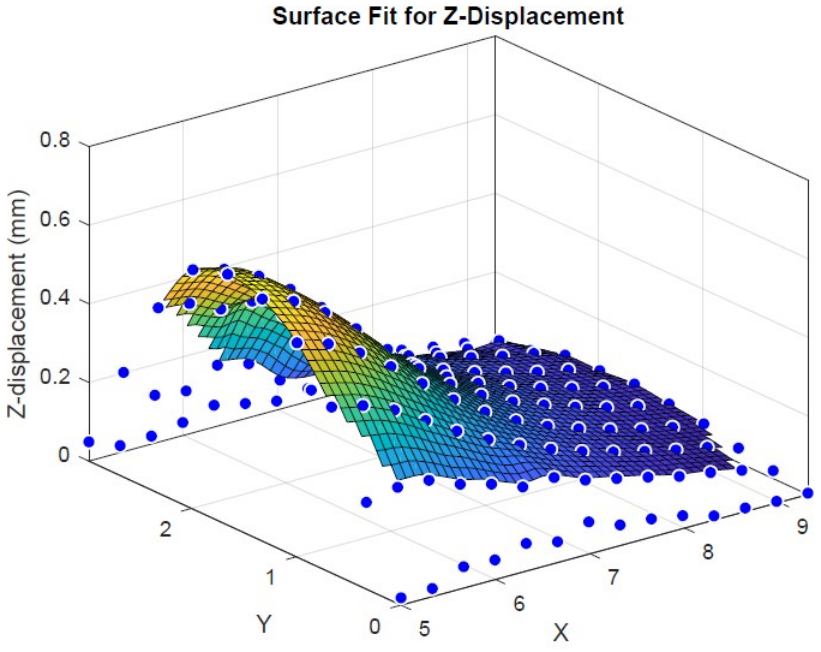

Figure 5.8: Displacement in Z-direction

5.4 Optimization Convergence

The optimization process was performed, using the fitted surfaces in Section 5.3, as explained in Chapter 4. The optimization process was repeated nine times, each time with different starting points. Table 5.3 shows the initial scaled values for the material constants ($SC10(I)$, $SC01(I)$, $SC11(I)$), the values to which each scaled material constant converged ($SC10(O)$, $SC01(O)$, $SC11(O)$), and the value of the root mean square error ($RMSE$) to which each run converged. Table 5.3 shows that the optimization process produced repeatable results from different starting points.

Table 5.3: Repetitive Optimization Starting Points and Results

♯	$SC10(I)$	$SC01(I)$	$SC11(I)$	$SC10(O)$	$SC01(O)$	$SC11(O)$	$RMSE$
1	5	10	10	30.5833	2.2048	3.0668	0.1559
2	9.4955	3.6716	4.9920	29.7409	2.2537	3.8309	0.1559
3	29.7359	2.2534	3.8308	29.7409	2.2537	3.8309	0.1559
4	15	15	15	36.0023	1.8205	4.2484	0.1560
5	36.0015	1.8204	4.2485	36.0020	1.8205	3.8236	0.1560
6	1.7491	1.9065	1.6136	23.6287	2.6724	3.9824	0.1562
7	23.6287	2.6724	3.9824	31.1299	2.1980	3.1032	0.1559
8	20	10	10	33.6646	1.9491	7.4461	0.1561
9	33.6643	1.9490	7.4461	33.6719	1.9495	6.7012	0.1561

Scaled material constants were calculated as shown in Equations 5.1 to 5.3.

$$SC10 = C10 \times 10^{-3} \tag{5.1}$$
$$SC01 = C01 \times 10^{-2} \tag{5.2}$$
$$SC11 = C11 \times 10^{-4} \tag{5.3}$$

To calculate the final material model, the averages of the material constants ($C10$, $C01$ and $C11$) from the optimization, where the $RMSE$ converged to 0.1559, were calculated. The final values for the Mooney-Rivlin constants are summarised in Table 5.4 and the evaluation of the resulting material model is discussed in Sections 5.5 and 5.6.

Table 5.4: Final Material Model

Variable	C10	C01	C11
Value	0.02974	0.02254	3.83086×10^{-4}

5.5 Optimization Performance

In this section, the results from using the material model in the finite element analysis (FEA) of the experimental geometry are discussed to evaluate whether the optimizer was effective in finding an accurate material model.

5.5.1 Displacements in the X-Direction (D_x)

Figure 5.9 shows the correlation coefficients (R^2 values) between the DIC data and the FEM results at each point on the surface of the sample for displacements in the x-direction.

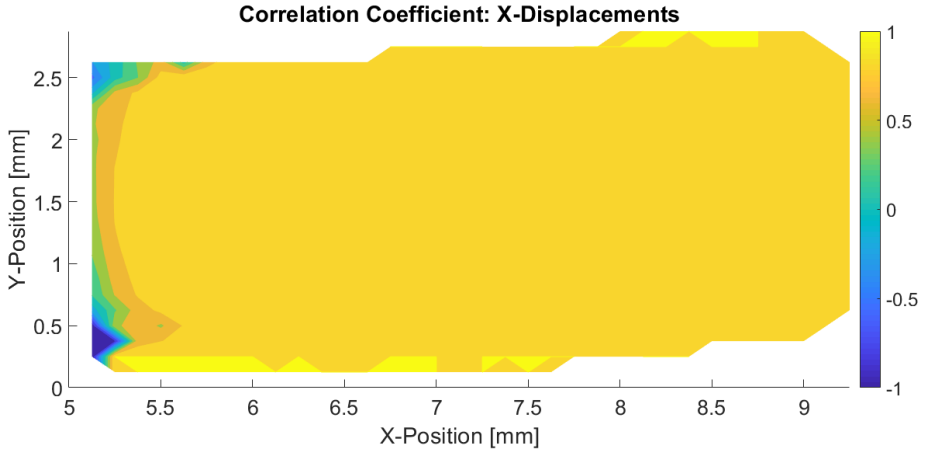

Figure 5.9: Correlation Coefficient for Dx

The average correlation coefficient across the surface of the sample for the x-displacements was calculated as $R^2 = 0.9492$. For perfect correlation between the experimental data and the FEM data, the correlation coefficient should be equal to 1. A correlation coefficient of -1 means that the values are the same, but the sign is opposite. It may be seen in Figure 5.9 that the values of displacement correlate well ($R^2 > 0.99$) for most of the sample surface. The physical values of the correlation coefficients are available in Appendix F.

Another observation from this figure is that the results correlated well near the bottom of the sample (where a glued contact condition was applied). This is an indication that the assumed boundary condition between the sample and the contact surface was reasonable.

Large errors in correlation are seen between $X = 5$ and $X = 5.5$. There is even a negative correlation between the values in small regions near the top and the bottom of the sample. This is the region in which tensile strains were expected in the x-direction and it seems that there are local areas in which the theoretical model could not predict the behaviour of the material successfully.

At $X = 5$ all values predicted by the FEM model were zero, which was to be expected from the imposed symmetry conditions. For this reason the correlation coefficient could not be computed in this region. Figure 5.10 shows the actual displacement values for both the FEM output and the measured results at this location. It may be seen that the difference between observed and predicted values had a maximum value of 0.07 mm, which was small enough to be seen as negligible.

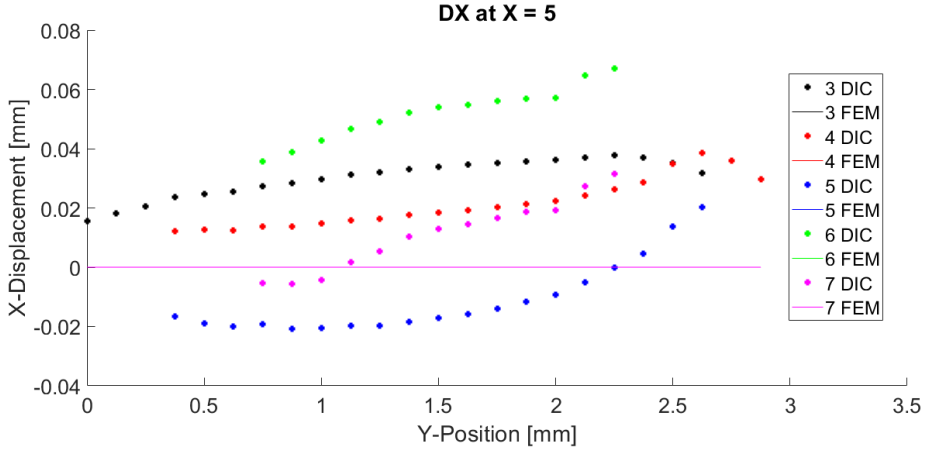

Figure 5.10: DX at X = 5

5.5.2 Displacements in the Z-Direction (D_z)

The correlation between the experimental and predicted displacements in the z-direction was the best out of all three directions. Here the average correlation coefficient over the surface of the sample was $R^2 = 0.9926$, which indicates good correlation between experimental and predicted results. Figure 5.11 shows the surface plot for the correlation coefficient of the z-displacements.

In the figure, it may be seen that the data correlates extremely well to predicted values for a significant part of the sample surface. Once again it may be seen that there is good correlation in areas where the glued boundary condition had a significant impact.

There is a small area of poor correlation in the top left corner where it was observed that the deformation of the sample was more complex than expected. There was a small 'fold' in the sample surface which was predicted by the FEM model as a phenomenon, however the predicted displacement values resulting from this effect were poorly predicted.

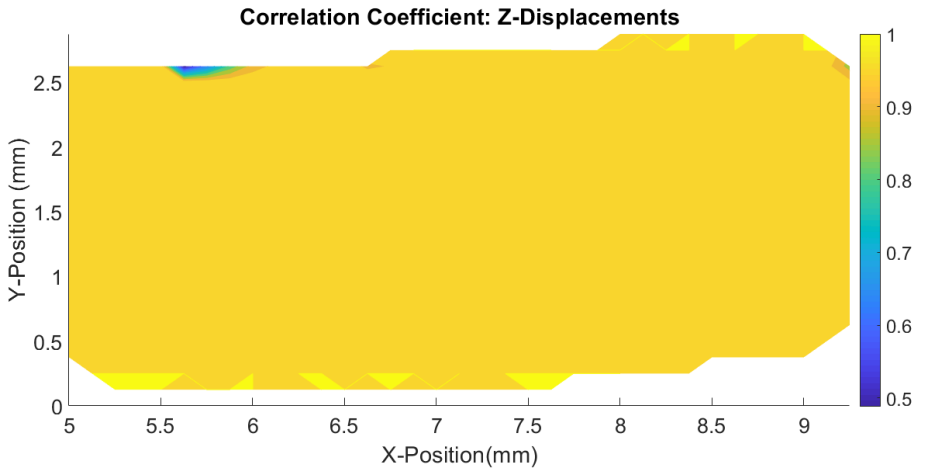

Figure 5.11: Correlation Coefficient for Dz

5.5.3 Displacements in the Y-Direction (D_y)

Figure 5.9 shows the correlation coefficients (R^2 values) between the DIC data and the FEM results at each point on the surface of the sample for displacements in the y-direction.

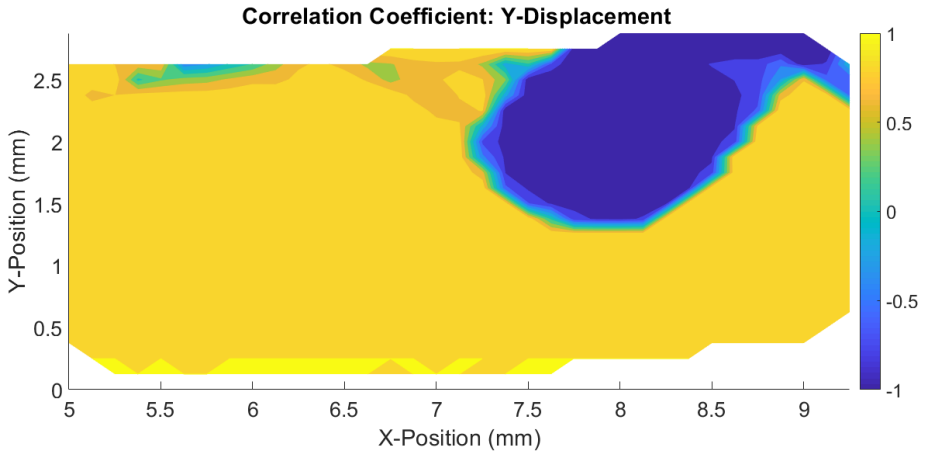

Figure 5.12: Correlation Coefficient for Dy

Once again it may be seen that the data correlated well to the predicted results near the area where a glued contact boundary condition was applied. However, it may be seen in this instance that there is a significant negative correlation between displacements in the top right corner of the sample.

Figure 5.13 shows the absolute displacements for both data sets at the top row of nodes on the sample surface. The FEM model predicted displacements close to zero, while the experimental data showed displacements in the negative y-direction.

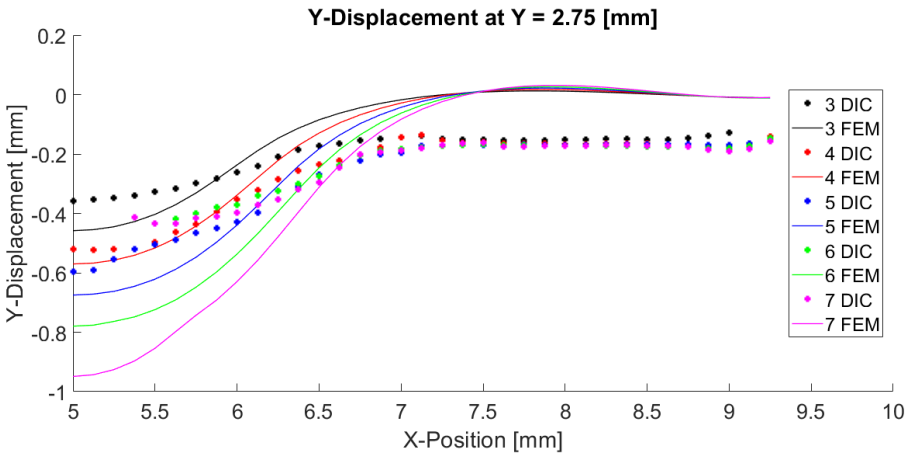

Figure 5.13: DY at Top of Sample Surface

Since only the front surface of the sample was used for experimental measurements, this phenomenon cannot be explained with complete certainty. However, with the use of the chosen material model, there is an inherent assumption of incompressibility of the material. It seems as though this assumption was not valid. Since the experimental results showed compression in the y-direction which is not seen in the FEM results while the displacements in x and z showed good correlation it is reasonable to speculate that there was compression in the sample material which was not predicted by the FEM model.

This may be the reason for the area of poor correlation seen in figure 5.12, however further testing would be necessary in order to make a final conclusion on the cause of the deviation.

The area directly under the pin ($X = 5$), where the deformations in the y-direction were larger shows better correlation when comparing experimental and theoretical displacements. In this area the correlation coefficient is larger than $R^2 = 0.95$, which is an acceptable value of the correlation coefficient.

The average correlation coefficient over the entire surface of the sample was poor due to the large area of negative correlation and had a value of $R^2 = 0.6092$, which is not an acceptable value for correlation between the experimental and theoretical results.

5.5.4 Summary of Displacement Results

Table 5.5 shows a summary of the average values for the correlation coefficient and the Root Mean Square Error (RMSE). When normalised over the maximum displacement value for each respective direction x, y, and z the RMSE corresponds to 7.22% of the Maximum x-displacement, 5.07% of the maximum z-displacement and 133.48% of the maximum y-displacement.

Even though the relative error percentages for displacements in x and z are below 10%, the errors in the y-direction are unacceptable.

Table 5.5: Summary of Average Correlation Coefficient and RMSE

Displacement Direction	Average Correlation Coefficient	RMSE [mm]
X	0.9492	0.041
Y	0.6092	0.144
Z	0.9926	0.04

From the results discussed in Sections 5.5.1 - 5.5.2 the following conclusions may be made:

1. The glued boundary condition applied to the bottom surface of the sample produced good correlation to experimental results and the glued contact assumption is therefore accepted.

2. The direction in which results were predicted most accurately was the out-of-plane direction, where experimental results and predicted results showed a significant correlation to each other.

3. The direction in which the predicted resulting deformation field was the most inaccurate was for displacements in the y-direction. The R^2 value for displacements in this direction was 0.6092, which is not acceptable. The error in this direction is extremely large and the results can not be seen as acceptable.

4. The displacements in the x-direction showed a correlation value of $R^2 = 0.9492$. Although this indicates that there is correlation between the experimental and predicted results, the aim in this research was to achieve a coefficient of at least 0.95.

5. The assumption of incompressibility may be inaccurate for this material, but it is not within the scope of this research to study the compressibility and additional testing would be needed to quantify the effect thereof.

Even though large errors were seen in this analysis, it is not possible to definitively say whether the optimizer itself performed well in terms of accuracy. If mistakes were made in assumptions regarding the material behaviour it would not be possible for the optimizer to find the perfect solution.

5.6 Validation of Material Model

This section discusses the results of the validation test. As discussed in Section 3.6 this test involved testing a different geometry of the same material to see whether or not the material model obtained from the FEM update method can successfully predict the behaviour of the material.

In the case of this research, a tensile test was chosen even though the test geometry was loaded in compression. This is seen as an extrapolation of the results, but seeing as the heart valve material for, which this test is being developed, usually undergoes both compression and tension cyclically the model would have to be able to predict both load cases successfully. From literature, it was learned that this may be possible by using a complex strain field in combination with the FEM update method (Garbowski *et al.*, 2012).

Figure 5.14 shows the correlation coefficients between the experimental results and the predicted behaviour as a contour plot over the surface of the sample. The R^2 value between the two sets of displacement values was calculated using multiple values for displacements at incremental forces for each DIC element on the surface of the sample. Since the FEM mesh was much finer than the DIC element size, FEM displacement values were mapped to the locations of DIC data points using linear interpolation.

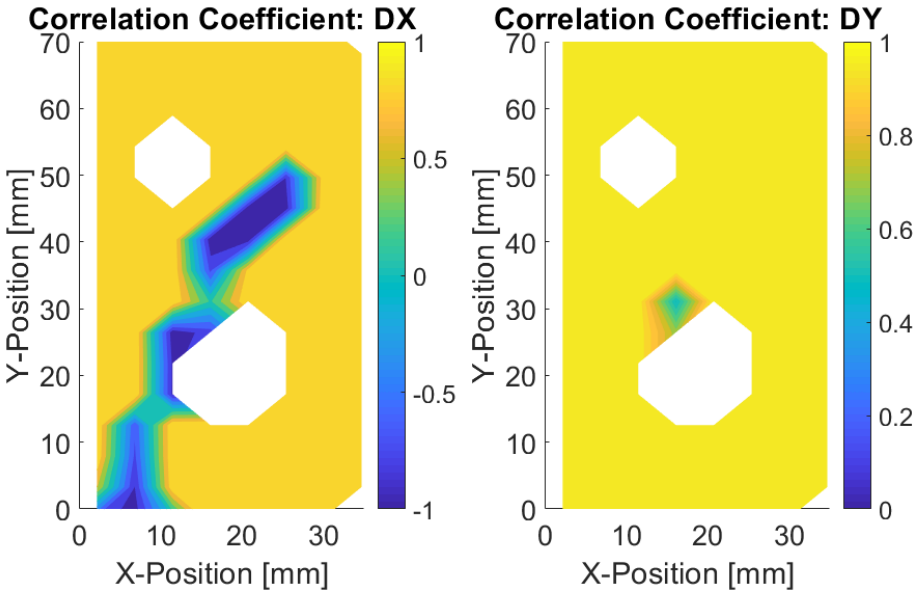

Figure 5.14: Correlation Coefficients

The average correlation coefficient for displacements in the x-direction was $R^2 = 0.7533$, which indicates a weak correlation. This value is not acceptable according to the design requirements defined in Chapter 3. It indicates that there is a weak correlation between the FEM results and the DIC data,

which means that the material model could not successfully predict the x-displacements of the sample under the described loading conditions.

The correlation coefficient for the y-displacements had an average value of $R^2 = 0.9806$, which is a strong correlation. This is surprising since the y-direction displacements are in the direction of the largest tensile force and the errors in the y-direction were larger than those in the x-direction. The difference in correlation coefficients between the x- and y-directions is most likely due to the large area where the correlation is negative for the x-displacement.

The average relative error was calculated as $\varepsilon_x = -2.2126$. The displacements in the y-direction produced even larger errors at a value of $\varepsilon_y = -3.0162$. The large negative values of this error indicate that the displacement observed during experimentation were significantly larger than those predicted by the FEM model, indicating that the material model obtained from the FEM update method was too stiff.

The absolute relative error had an average value of $\varepsilon_{xabs} = 4.3363$ and $\varepsilon_{yabs} = 3.0512$ in the x- and y- directions respectively. These error values are too large for the material model to be accepted as an accurate predictive model for the behaviour of the material.

Chapter 6

Conclusion and Recommendations

6.1 Conclusion

The motivation for this research was to design and test an experimental method which would be applicable to testing heart valve tissue at a scale of 4 mm X 4 mm X 1-2 mm. In order to use the available equipment for the research, however the method was tested at a larger scale.

Five objectives were set in Chapter 1 and in Section 3.2.1 8 design requirements were defined, which would serve as guidelines for the design of the experimental method. Table 6.1 shows a summary of the level to which each design requirement was met.

The design of the test geometry (compressive force applied by a pin) was implemented in a robust inverse FEM update method since the simple geometry and boundary conditions could be easily implemented in an FEA, however there was a large error (>100%) in the prediction of y-displacements as discussed in Section 5.5.3.

The relative error of the x- and y-displacements were both lower than 10%, but the correlation coefficient in the x-direction was not high enough according to the criteria in the design requirements. It was concluded that the calculated material model was not accurate.

It should, however be noted that the significant error in displacement values in the y-direction (Please see Figuires 5.12 and 5.13) seems to be due to an error in the assumption of incompressibility. It is therefor not possible to dissmiss the experimental method itsself as inaccurate.

The validation test case showed that the resulting material model did not extrapolate well to tensile strains. Once again the predicted displacements were not accurate, in fact, the displacements predicted by the FEM model were on average less than half the displacements observed from experimentation.

Table 6.1: Achievement of Design Requirements

No.	Requirement	Achieved	Degree to which objective was fulfilled
1	The method must avoid stress concentrations and gripping	Yes	No Stress concentrations or gripping effects were introduced during testing.
2	It must be possible to implement the method at a 4 mm scale	Partially	Method could not be proven completely unviable, but would pose serious challenges at a 4 mm scale.
3	Sample size for this research must be smaller than 12 mm x 12 mm x 3-6 mm.	Yes	Samples in this research were 10 mm x 10 mm x 2.7 mm.
4	The method of measurement must not affect the material behaviour	Yes	Non-Contact method of strain measurement was implemented
5	Sample must have a complex strain field	Yes	Three dimensional strain field was achieved with varying relative directional strains.
6	Data is usable in FEM update method, at least 500 datapoints	Yes	Experimental data contained 840 data points and could be used in the FEM update method.
7	Duplicate the test geometry in a robust FEM model	Partially	Boundary conditions were accurately reproduced, model could compute strains for different material parameters, however there was a significant error in the predicted displacement field for y-displacements.
8	Validation test must show that displacements can be predicted to an error of less than 10% and correlation coefficient larger than 0.95.	No	Large errors were observed in both directions considered in the validation test. X-showed poor correlation although y-displacements showed good correlation.

The repeatability was also evaluated. It was found that the raw data showed deviation in force measurements of up to 11.34%. However, the optimization algorithm produced repeatable results at various different starting points, with the RMSE to which it converged showing a spread of results of only 0.0003 mm.

6.2 Recommendations for future research

To increase the deformation features, which may be useful in the optimization process it is suggested that the pin geometry should be refined. The pin should not extend past the observation surface as this causes areas of the sample to become obscured by the equipment as was observed in this research. It is possible that the areas of the sample where no deformation could be measured could contribute to improving the accuracy of the inverse.

In this research, the chosen material model was the 3-parameter Mooney-Rivlin model, since the model is easily implemented, well studied, and has been proven able to produce accurate predictions for the deformation of silicone-rubbers in previous studies. It is possible that better results could be obtained using a different material model. Perhaps future research could include more than one option for a material model and study other material properties such as compressibility.

Appendices

Appendix A

Lens Calculations

A.1 Theory

First, the hyperfocal distance (HFD) must be calculated using Equation A.1. This is the closest distance to the camera (which is in focus) when the camera is focussed on infinity. Here, CoC is the size of the circle of confusion of the sensor, FL is the focal length of the lens and F_{stop} represents the aperture of the lens expressed as an F-stop value (the ratio between the focal length and the aperture).

$$HFD = \frac{FL^2}{f_{stop}CoC} \tag{A.1}$$

The circle of confusion is the diameter of the spot where light converges on the sensor. The size of the circle of confusion can be approximated using the Zeiss Formula (Equation A.2) if it is not specified by the lens datasheet. In this formula d_s is the diagonal size of the sensor as specified in the sensor datasheet.

$$CoC = \frac{d_s}{1500} \tag{A.2}$$

After calculating the HFD, the nearest and furthest points of the depth of field are determined. These values depend on the hyperfocal distance, object distance (OD) and the focal length of the lens (FL) as shown in Equation A.3 and Equation A.4 (Reu, 2013*a*).

$$D_{near} = \frac{HFD * OD}{HFD + (OD - FL)} \tag{A.3}$$

$$D_{far} = \frac{HFD * OD}{HFD - (OD - FL)} \tag{A.4}$$

Where D_{near} and D_{far} are the closest and furthest distances of the depth of field respectively. The size of the field of view (FOV) is also the size of the scale of observation to be captured in an image. It can be calculated using Equation A.5 (Reu, 2012*a*).

$$FOV = \frac{d_s * OD}{FL} \tag{A.5}$$

Now that the depth of field is known, another consideration is the resolution of the captured image. The FOV will help determine if the researcher can capture a sample with a high enough resolution to successfully identify enough elements, each at least 30 pixels in size, as discussed in Section 2.6.1. First, the correct lens is chosen, then the resulting resolution is checked.

The field of view is calculated in terms of the length of the diagonal of the image, for which it is necessary to calculate the horizontal and vertical dimensions. Figure A.1 shows how the field of view is measured. The aspect ratio (AR) of the sensor determines the ratio between the vertical and horizontal dimensions of the image (Reu, 2012*a*). These dimensions are calculated using trigonometric equations (Equation A.6 to A.8).

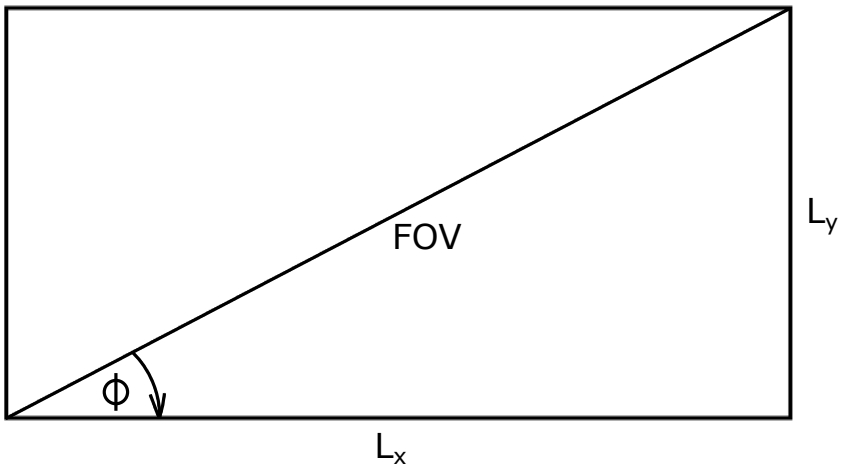

Figure A.1: Field of view and Aspect Ratio

$$AR = \frac{L_y}{L_x} \tag{A.6}$$

$$\phi = \arctan(AR)$$

$$L_x = FoV * \cos\phi \tag{A.7}$$

$$L_y = FoV * \sin\phi \tag{A.8}$$

Extra considerations must be made to account for the angle between the camera and the sample. This angle (Figure A.2) is a result of using two cameras in order to obtain measurements in three directions. Here, B (Equation A.9) must be smaller than half of the depth of field to make sure all extremities of the sample will be in focus. A (Equation A.10) is the projected size of the sample on the focal plane of the camera, which is used to determine the number of pixels on the sample in an image.

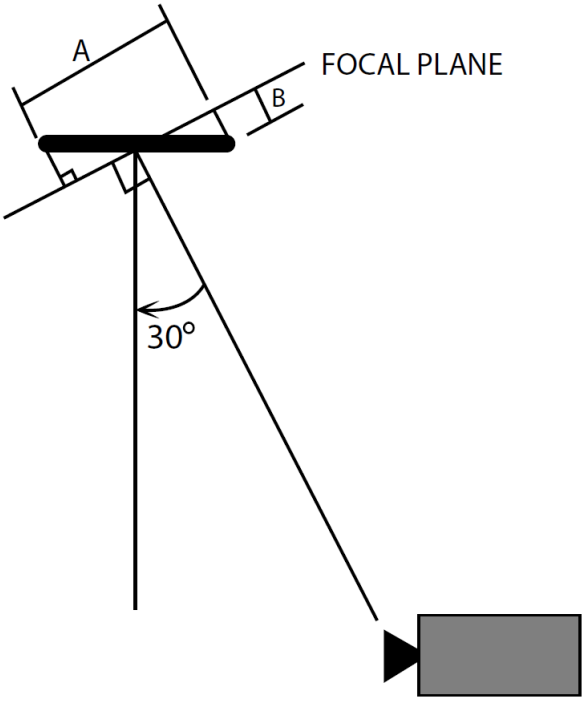

Figure A.2: Sample at an Angle to Focal Plane

$$B = \frac{sample_x}{2} * \sin\phi \tag{A.9}$$

$$A = sample_x * \cos\phi \tag{A.10}$$

Each pixel has a dimension in the horizontal direction (x) and the vertical direction (y) and since the number of pixels in each direction is known from the sensor datasheet, the size of each pixel can be calculated using equations A.11 and A.12. Here, P_x and P_y are the horizontal and vertical sizes of a pixel, respectively.

$$P_x = \frac{L_x}{2448} \tag{A.11}$$

$$P_y = \frac{L_y}{2050} \tag{A.12}$$

Next, the number of pixels, that fit into the area of the image where the sample is placed, is calculated. This is an important parameter since there must be enough pixels in the sample area to create a sufficient number of 30 pixel DIC elements to generate enough data points for the inverse method. Equations A.13 to A.14 are used to calculate the number of pixels that will fall within the sample.

$$N_x = \frac{A}{P_x} \tag{A.13}$$

$$N_y = \frac{Sample_y}{P_y} \tag{A.14}$$

N_x and N_y are the number of pixels on the surface of the sample in the horizontal and vertical directions, respectively. The size of the sample does not need to be corrected in the y-direction since there is no angle between the camera and the surface of the sample in this plane.

A.2 Sample Lens Calculations

Lens Make and Model: Edmund Optics Double Gauss

The values used in these calculations are applicable to the chosen set of lenses:

$$\begin{aligned} d &= 6\ mm \\ FL &= 75\ mm \\ OD &= 500\ mm \\ F_{stop} &= 30 \end{aligned}$$

First, calculate the size of the circle of confusion.

$$CoC = \frac{d}{1500} = 0.004\ mm$$

Next, the hyperfocal distance can be calculated:

$$HFD = \frac{FL^2}{F_{stop} \times CoC} = 46.875\ m \tag{A.15}$$

This distance is the distance at from where focus will be perfect when the lens is focused on infinity. It is used to calculate the depth of field by first calculating the furthest and closest points where there is acceptable focus. These three distances were calculated as follows:

$$\begin{aligned} D_{near} &= \frac{HFD \times OD}{HFD + (OD - FL)} = 495.5074\ mm \\ D_{far} &= \frac{HFD \times OD}{HFD - (OD - FL)} = 504.5748\ mm \\ DOF &= D_{far} - D_{near} = 9.0674mm \end{aligned}$$

Lastly it must be verified whether or not the field of view at this depth of field is adequate:

$$FOV = \frac{d \times OD}{FL} = 40\ mm$$

The field of view and depth of field were the variables which determined which lens set is best for this purpose, but do not indicate whether or not the selected set is good enough in terms of the DIC process. To determine the quality of this lens set in terms of DIC.

First, the size of the field of view is calculated in physical space using the aspect ratio of the sensor.

$$\begin{aligned} AR &= \frac{L_y}{L_x} = \frac{6}{5} \\ \phi &= \arctan(AR) = 39.8^\circ \\ L_x &= FoV * \cos\phi = 30.73\ mm \\ L_y &= FoV * \sin\phi = 25.61\ mm \end{aligned}$$

Next variables A and B as discribed in section 2.6.3 and the sizes of each pixel in the x- and y-direction respectively.

$$B = \frac{sample_x}{2} * \sin\phi = 2.5\ mm$$
$$A = sample_x * \cos\phi = 8.66\ mm$$
$$P_x = \frac{L_x}{2448} = 0.0109\ mm$$
$$P_y = \frac{L_y}{2050} = 0.0125\ mm$$

Lastly, the amount of pixels on the surface of the sample, which are available for use in DIC is calculated.

$$NP_x = \frac{A}{P_x} = 796\ pixels$$
$$NP_y = \frac{Sample_y}{P_y} = 400.32\ pixels$$

To calculate the amount of subsets (30 pixels each) the amount of pixels in the x-direction is divided by six and the amount of pixels in the y-direction by five.

$$Subsets_x = 132$$
$$Subsets_y = 80$$
$$Total\ amount\ of\ subsets = Subsets_x \times Subsets_y = 10560$$

This amount of subsets is a theoretical estimation. 10560 data points would be too many to use in the numerical simulation, but this theoretical value allows for a large safety factor for the actual amount of data points to be adequate even if the theoretical amount is not reached.

Appendix B

Engineering Drawings

B.0.1 Sample Mold Geometry

This page is intentionally left blank.

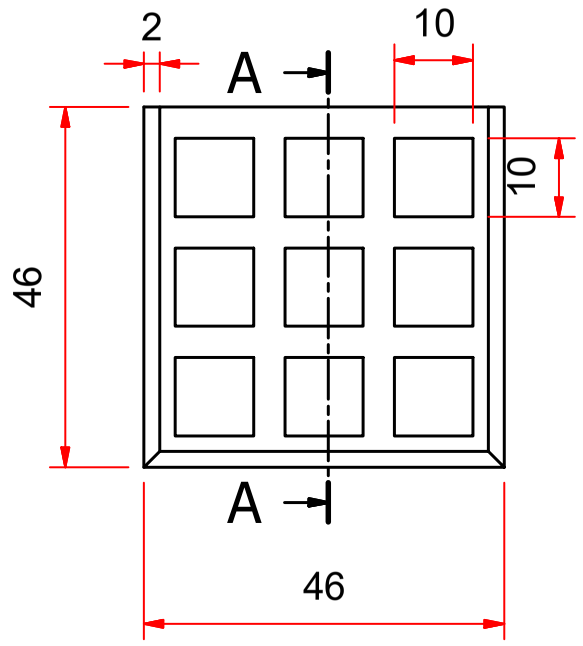

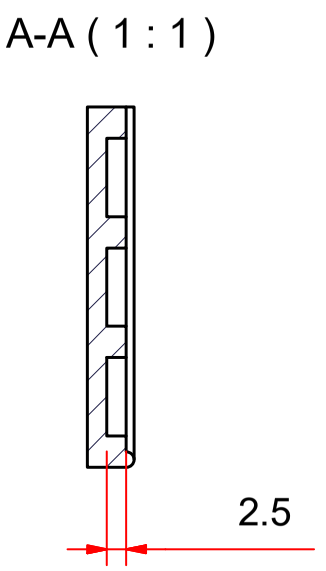

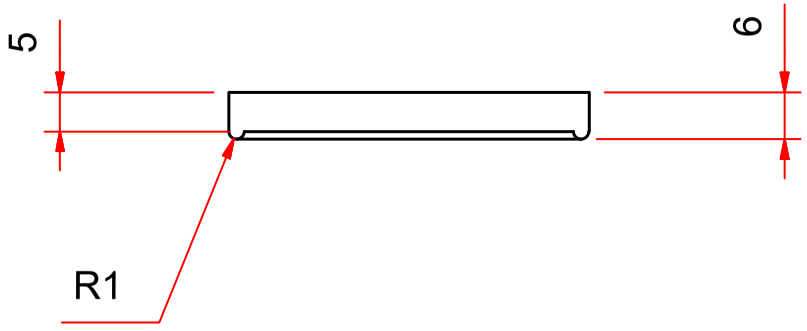

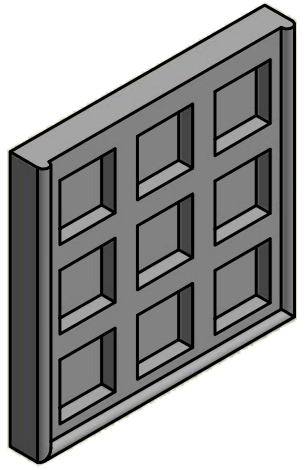

ITEM	BESKRYWING	AANTAL	MATERIAAL / SPESIFIKASIES

UNIVERSITEIT VAN STELLENBOSCH

SKAAL OP A	1:1	TITEL:	SAMPLE MOLD
MATE IN	mm		
STUDENTE No. 16969464	TEKENAAR MC VILJOEN	NAGESIEN	
DATUM 2017/07/20	VEL No. 1 VAN 1 VELLE	No.	1/2/2017

B.0.2 Pin Geometry

This page is intentionally left blank.

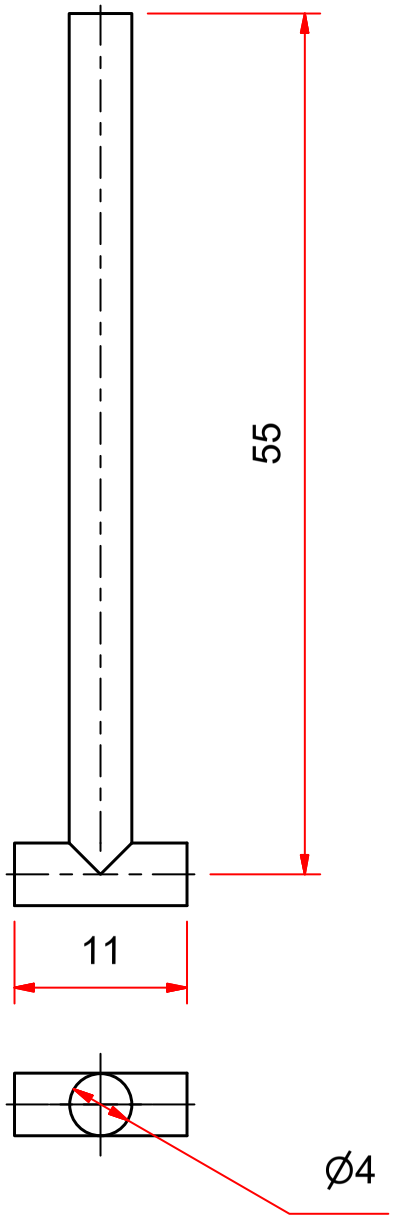

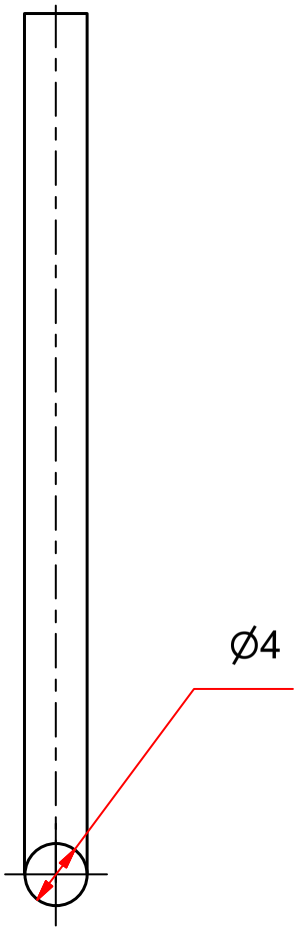

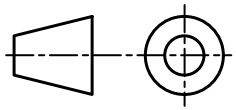

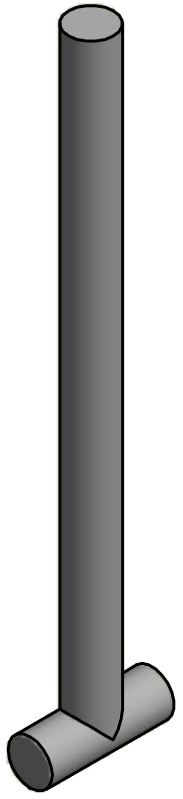

ITEM	BESKRYWING	AANTAL	MATERIAAL / SPESIFIKASIES

UNIVERSITEIT VAN STELLENBOSCH

SKAAL OP A	2:1	TITEL:	4 MM PIN						
MATE IN	mm								
STUDENTE No.	16969464	TEKENAAR	MC VILJOEN	NAGESIEN	DATUM	20/07/2017	VEL No. 1	VAN 1	VELLE	No.	1/1/2017

Appendix C

Material Data Sheet

Material Datasheet Source: Smooth-On (n.d.)

This page in intentionally left blank.

Ecoflex® Series

Super-Soft, Addition Cure Silicone Rubbers

Cured Material! Certified Skin Safe!

www.smooth-on.com

PRODUCT OVERVIEW

Ecoflex® rubbers are platinum-catalyzed silicones that are versatile and easy to use. **Ecoflex®** rubbers are mixed 1A:1B by weight or volume and cured at room temperature with negligible shrinkage. Low viscosity ensures easy mixing and de-airing, or you can choose to mix and dispense using our convenient dispensing cartridges. Cured material is skin safe and certified by an independent laboratory to ISO 10993-10, Biological evaluation of medical devices, Part 10: Tests for irritation and skin sensitization.

Cured rubber is very soft, very strong and very "stretchy", stretching many times its original size without tearing and will rebound to its original form without distortion. **Ecoflex®** rubbers are water white translucent and can be color pigmented with Silc Pig® pigments for creating a variety of color effects. You can also add Smooth-On's Silicone Thinner® to further lower the viscosity. THI-VEX® silicone thickener can be added by weight to Ecoflex® silicones for brushable aplications.

Soft, Softer, Softest . . . **Ecoflex®** rubbers are based on Smooth-On's Dragon Skin® technology and are currently available in four different hardness': Shore A-5, Shore 00-10, 00-20, 00-30 and 00-50. They are suitable for a variety of applications including making prosthetic appliances, cushioning for orthotics and special effects applications (especially in animatronics where repetitive motion is required). **Ecoflex® 5** has a pot life of 1 minute and a demold time of 5 minutes – Available only in dispensing cartridges.

Note: Ecoflex® 00-10 cures with a "tacky" surface.

TECHNICAL OVERVIEW

	Mixed Viscosity (ASTM D-2393)	Specific Gravity (g/cc) (ASTM D-1475)	Specific Volume (cu. in./lb.) (ASTM D-1475)	Pot Life (ASTM D-2471)	Cure Time	Shore Hardness (ASTM D-2240)	Tensile Strength (ASTM D-412)	100% Modulus (ASTM D-412)	Elongation at Break % (ASTM D-412)	Die B Tear Strength (ASTM D-624)	Shrinkage (in./in.) (ASTM D-2566)
Ecoflex® 5	13,000 cps	1.07	25.8	1 min.	5 min.	5A	350 psi	15 psi	1000%	75 pli	< .001 in./in.
Ecoflex® 00-50	8,000 cps	1.07	25.9	18 min.	3 hours	00-50	315 psi	12 psi	980%	50 pli	< .001 in./in.
Ecoflex® 00-30	3,000 cps	1.07	26.0	45 min.	4 hours	00-30	200 psi	10 psi	900%	38 pli	< .001 in./in.
Ecoflex® 00-20	3,000 cps	1.07	26.0	30 min.	4 hours	00-20	160 psi	8 psi	845%	30 pli	< .001 in./in.
Ecoflex® 00-10	14,000 cps	1.04	26.6	30 min.	4 hours	00-10	120 psi	8 psi	800%	22 pli	< .001 in./in.

*All values measured after 7 days at 73°F/23°C

Mix Ratio: 1A:1B by volume or weight
Color: Translucent
Useful Temperature Range: -65°F to 450°F (-53°C to 232°C)
Dielectric Strength (ASTM D-147-97a)***:*** >350 volts/mil

PROCESSING RECOMMENDATIONS

PREPARATION... Safety – Use in a properly ventilated area ("room size" ventilation). Wear safety glasses, long sleeves and rubber gloves to minimize contamination risk. Wear vinyl gloves only. Latex gloves will inhibit the cure of the rubber.

Store and use material at room temperature (73°F/23°C). Warmer temperatures will drastically reduce working time and cure time. Storing material at warmer temperatures will also reduce the usable shelf life of unused material. These products have a limited shelf life and should be used as soon as possible.

Cure Inhibition – Addition-cure silicone rubber may be inhibited by certain contaminants in or on the pattern to be molded resulting in tackiness at the pattern interface or a total lack of cure throughout the mold. Latex, tin-cure silicone, sulfur clays, certain wood surfaces, newly cast polyester, epoxy, tin cure silicone rubber or urethane rubber may cause inhibition. If compatibility between the rubber and the surface is a concern, a small-scale test is recommended. Apply a small amount of rubber onto a non-critical area of the pattern. Inhibition has occurred if the rubber is gummy or uncured after the recommended cure time has passed.

Because no two applications are quite the same, a small test application to determine suitability for your project is recommended if performance of this material is in question.

To prevent inhibition, one or more coatings of a clear acrylic lacquer applied to the model surface is usually effective. Allow any sealer to thoroughly dry before applying rubber. Note: Even with a sealer, platinum silicones will not work with modeling clays containing heavy amounts of sulfur. Do a small scale test for compatibility before using on your project.

Appendix D

Correlation Coefficient Values for Test Case

Correlation Coefficient Values Between Experimental and FEM X-Displacements

	1	2	3	4	5	6
1	NaN	NaN	NaN	NaN	NaN	NaN
2	NaN	NaN	NaN	NaN	NaN	NaN
3	NaN	NaN	NaN	NaN	NaN	NaN
4	NaN	NaN	NaN	NaN	NaN	NaN
5	NaN	NaN	NaN	NaN	0.5607	0.8144
6	NaN	-0.1080	0.3721	0.7002	0.8421	0.9107
7	NaN	0.2098	0.6087	0.8179	0.8973	0.9428
8	NaN	0.2538	0.6894	0.8536	0.9218	0.9568
9	NaN	0.3541	0.7351	0.8762	0.9350	0.9629
10	NaN	0.4335	0.7697	0.8912	0.9415	0.9658
11	NaN	0.4825	0.7923	0.8993	0.9446	0.9666
12	NaN	0.5269	0.8054	0.9033	0.9455	0.9668
13	NaN	0.5459	0.8087	0.9027	0.9449	0.9661
14	NaN	0.5468	0.8055	0.9008	0.9433	0.9653
15	NaN	0.5513	0.8038	0.8961	0.9407	0.9634
16	NaN	0.5497	0.7892	0.8875	0.9353	0.9607
17	NaN	0.5237	0.7743	0.8781	0.9313	0.9583
18	NaN	0.5655	0.7631	0.8663	0.9215	0.9586
19	NaN	0.5464	0.7408	0.8499	0.9245	0.9595
20	NaN	NaN	0.6573	0.8448	0.9349	0.9726
21	NaN	NaN	NaN	NaN	NaN	0.9675
22	NaN	NaN	NaN	NaN	NaN	NaN
23	NaN	NaN	NaN	NaN	NaN	NaN
24	NaN	NaN	NaN	NaN	NaN	NaN

Correlation Coefficient Values Between Experimental and FEM Y-Displacements

	1	2	3	4	5	6
1	NaN	NaN	NaN	NaN	NaN	NaN
2	NaN	NaN	NaN	NaN	NaN	NaN
3	NaN	NaN	NaN	NaN	NaN	NaN
4	NaN	NaN	NaN	NaN	NaN	NaN
5	NaN	NaN	NaN	NaN	0.9939	0.9932
6	NaN	0.9965	0.9956	0.9950	0.9942	0.9929
7	0.9982	0.9975	0.9966	0.9959	0.9948	0.9934
8	0.9989	0.9984	0.9976	0.9967	0.9953	0.9938
9	0.9995	0.9990	0.9981	0.9969	0.9954	0.9937
10	0.9993	0.9987	0.9977	0.9964	0.9945	0.9927
11	0.9989	0.9983	0.9972	0.9956	0.9937	0.9914
12	0.9983	0.9977	0.9964	0.9947	0.9924	0.9899
13	0.9981	0.9973	0.9959	0.9939	0.9914	0.9884
14	0.9974	0.9966	0.9949	0.9928	0.9899	0.9867
15	0.9973	0.9965	0.9947	0.9925	0.9899	0.9856
16	0.9968	0.9959	0.9939	0.9923	0.9886	0.9843
17	0.9942	0.9926	0.9905	0.9882	0.9845	0.9798
18	0.9799	0.9801	0.9786	0.9794	0.9755	0.9678
19	0.9281	0.9390	0.9524	0.9578	0.9537	0.9435
20	NaN	NaN	0.7976	0.8652	0.8797	0.8952
21	NaN	NaN	NaN	NaN	NaN	0.4740
22	NaN	NaN	NaN	NaN	NaN	NaN
23	NaN	NaN	NaN	NaN	NaN	NaN
24	NaN	NaN	NaN	NaN	NaN	NaN

Correlation Coefficient Values Between Experimental and FEM Z-Displacements

	1	2	3	4	5	6
1	NaN	NaN	NaN	NaN	NaN	NaN
2	NaN	NaN	NaN	NaN	NaN	NaN
3	NaN	NaN	NaN	NaN	NaN	NaN
4	NaN	NaN	NaN	NaN	NaN	NaN
5	NaN	NaN	NaN	NaN	0.9992	0.9992
6	NaN	0.9983	0.9988	0.9993	0.9997	0.9995
7	0.9988	0.9990	0.9994	0.9995	0.9995	0.9992
8	0.9985	0.9987	0.9987	0.9986	0.9987	0.9984
9	0.9984	0.9983	0.9982	0.9980	0.9979	0.9977
10	0.9987	0.9987	0.9983	0.9981	0.9980	0.9975
11	0.9993	0.9991	0.9987	0.9984	0.9979	0.9974
12	0.9995	0.9993	0.9989	0.9985	0.9980	0.9974
13	0.9996	0.9993	0.9990	0.9986	0.9981	0.9974
14	0.9997	0.9995	0.9992	0.9988	0.9982	0.9974
15	0.9997	0.9995	0.9993	0.9990	0.9984	0.9978
16	0.9997	0.9996	0.9995	0.9993	0.9988	0.9984
17	0.9997	0.9997	0.9996	0.9993	0.9989	0.9983
18	1.0000	0.9999	0.9995	0.9985	0.9974	0.9961
19	0.9993	0.9993	0.9982	0.9963	0.9940	0.9909
20	NaN	NaN	0.9968	0.9979	0.9958	0.9913
21	NaN	NaN	NaN	NaN	NaN	0.9901
22	NaN	NaN	NaN	NaN	NaN	NaN
23	NaN	NaN	NaN	NaN	NaN	NaN
24	NaN	NaN	NaN	NaN	NaN	NaN

Appendix E

Root Mean Square Error Values for Test Case

RMSE for Dx

	1	2	3	4	5	6
1	NaN	NaN	NaN	NaN	NaN	NaN
2	NaN	NaN	NaN	NaN	NaN	NaN
3	NaN	NaN	NaN	NaN	NaN	NaN
4	NaN	NaN	NaN	NaN	NaN	NaN
5	NaN	NaN	NaN	NaN	0.0352	0.0317
6	NaN	0.0246	0.0256	0.0257	0.0272	0.0286
7	0.0229	0.0218	0.0222	0.0227	0.0253	0.0266
8	0.0243	0.0224	0.0216	0.0223	0.0244	0.0256
9	0.0260	0.0227	0.0214	0.0219	0.0236	0.0253
10	0.0276	0.0233	0.0215	0.0220	0.0240	0.0262
11	0.0287	0.0238	0.0218	0.0225	0.0249	0.0275
12	0.0303	0.0247	0.0223	0.0231	0.0258	0.0289
13	0.0312	0.0252	0.0226	0.0237	0.0270	0.0305
14	0.0317	0.0255	0.0229	0.0241	0.0277	0.0315
15	0.0325	0.0262	0.0231	0.0242	0.0278	0.0317
16	0.0331	0.0268	0.0236	0.0241	0.0274	0.0310
17	0.0333	0.0275	0.0241	0.0236	0.0260	0.0294
18	0.0372	0.0338	0.0278	0.0259	0.0270	0.0268
19	0.0391	0.0345	0.0298	0.0277	0.0249	0.0249
20	NaN	NaN	0.0229	0.0200	0.0188	0.0189
21	NaN	NaN	NaN	NaN	NaN	0.0092
22	NaN	NaN	NaN	NaN	NaN	NaN
23	NaN	NaN	NaN	NaN	NaN	NaN
24	NaN	NaN	NaN	NaN	NaN	NaN

RMSE for Dy

	1	2	3	4	5	6
1	NaN	NaN	NaN	NaN	NaN	NaN
2	NaN	NaN	NaN	NaN	NaN	NaN
3	NaN	NaN	NaN	NaN	NaN	NaN
4	NaN	NaN	NaN	NaN	NaN	NaN
5	NaN	NaN	NaN	NaN	0.0878	0.0902
6	NaN	0.0808	0.0829	0.0856	0.0881	0.0912
7	0.0761	0.0763	0.0786	0.0819	0.0848	0.0892
8	0.0722	0.0723	0.0754	0.0793	0.0837	0.0889
9	0.0653	0.0658	0.0692	0.0738	0.0789	0.0852
10	0.0596	0.0602	0.0638	0.0692	0.0750	0.0826
11	0.0517	0.0522	0.0563	0.0620	0.0688	0.0771
12	0.0452	0.0458	0.0496	0.0555	0.0627	0.0722
13	0.0380	0.0385	0.0414	0.0472	0.0550	0.0651
14	0.0338	0.0338	0.0356	0.0404	0.0480	0.0587
15	0.0313	0.0305	0.0303	0.0330	0.0396	0.0506
16	0.0321	0.0314	0.0287	0.0279	0.0335	0.0437
17	0.0420	0.0413	0.0359	0.0309	0.0303	0.0363
18	0.0609	0.0581	0.0517	0.0395	0.0346	0.0354
19	0.0968	0.0921	0.0766	0.0642	0.0541	0.0449
20	NaN	NaN	0.1411	0.1246	0.1109	0.0917
21	NaN	NaN	NaN	NaN	NaN	0.2101
22	NaN	NaN	NaN	NaN	NaN	NaN
23	NaN	NaN	NaN	NaN	NaN	NaN
24	NaN	NaN	NaN	NaN	NaN	NaN

RMSE for Dx

	1	2	3	4	5	6
1	NaN	NaN	NaN	NaN	NaN	NaN
2	NaN	NaN	NaN	NaN	NaN	NaN
3	NaN	NaN	NaN	NaN	NaN	NaN
4	NaN	NaN	NaN	NaN	NaN	NaN
5	NaN	NaN	NaN	NaN	0.0927	0.0926
6	NaN	0.1002	0.1017	0.1024	0.1040	0.1054
7	0.0945	0.0985	0.1006	0.1007	0.1022	0.1035
8	0.0919	0.0959	0.0960	0.0959	0.0976	0.0983
9	0.0850	0.0881	0.0887	0.0891	0.0904	0.0910
10	0.0810	0.0846	0.0850	0.0847	0.0859	0.0858
11	0.0777	0.0807	0.0801	0.0798	0.0800	0.0797
12	0.0729	0.0757	0.0756	0.0751	0.0750	0.0744
13	0.0691	0.0720	0.0713	0.0700	0.0696	0.0688
14	0.0654	0.0677	0.0666	0.0654	0.0648	0.0637
15	0.0615	0.0638	0.0633	0.0612	0.0601	0.0590
16	0.0586	0.0609	0.0586	0.0561	0.0552	0.0535
17	0.0561	0.0577	0.0560	0.0540	0.0526	0.0504
18	0.0551	0.0572	0.0547	0.0513	0.0501	0.0470
19	0.0593	0.0587	0.0530	0.0506	0.0489	0.0454
20	NaN	NaN	0.0462	0.0426	0.0417	0.0380
21	NaN	NaN	NaN	NaN	NaN	0.0455
22	NaN	NaN	NaN	NaN	NaN	NaN
23	NaN	NaN	NaN	NaN	NaN	NaN
24	NaN	NaN	NaN	NaN	NaN	NaN

Appendix F

Correlation Coefficient Values for Validation Case

Correlation Coefficient Values Between Experimental and FEM X-Displacements

	1	2	3	4	5	6
1	NaN	-0.6949	-0.9099	-0.0439	0.9964	0.9880
2	NaN	0.6010	-0.8249	0.9440	0.9987	0.9940
3	NaN	0.9658	-0.6624	0.9892	0.9987	0.9977
4	NaN	0.9900	-0.5836	0.9798	0.9985	0.9978
5	NaN	0.9900	0.9861	-0.8689	NaN	NaN
6	NaN	0.9899	0.9913	-0.8606	NaN	NaN
7	NaN	0.9893	0.9883	-0.9515	-0.7040	NaN
8	NaN	0.9909	0.9888	0.9865	0.1591	0.9913
9	NaN	0.9934	0.9934	0.9937	-0.6722	0.8451
10	NaN	0.9951	0.9956	0.9853	-0.9591	-0.9633
11	NaN	0.9960	0.9962	0.9885	0.9907	-0.9788
12	NaN	0.9964	0.9963	NaN	0.9944	0.9945
13	NaN	0.9961	0.9962	NaN	0.9952	0.9948
14	NaN	0.9946	0.9947	0.9953	0.9955	0.9949
15	NaN	0.9935	0.9936	0.9940	0.9948	0.9947
16	NaN	0.9924	0.9928	0.9924	0.9926	0.9935
17	NaN	0.9917	0.9926	0.9917	0.9870	0.9911

Correlation Coefficient Values Between Experimental and FEM Y-Displacements

	1	2	3	4	5	6
1	NaN	0.9877	0.9879	0.9880	0.9881	0.9880
2	NaN	0.9877	0.9879	0.9880	0.9881	0.9879
3	NaN	0.9877	0.9878	0.9880	0.9881	0.9879
4	NaN	0.9877	0.9878	0.9879	0.9880	0.9879
5	NaN	0.9877	0.9877	0.9877	NaN	NaN
6	NaN	0.9876	0.9877	0.9876	NaN	NaN
7	NaN	0.9876	0.9876	0.9876	0.7159	NaN
8	NaN	0.9875	0.9875	0.9880	0.4857	0.9867
9	NaN	0.9873	0.9875	0.9888	0.9867	0.9868
10	NaN	0.9871	0.9875	0.9809	0.9868	0.9868
11	NaN	0.9870	0.9876	0.9910	0.9867	0.9866
12	NaN	0.9869	0.9879	NaN	0.9865	0.9863
13	NaN	0.9873	0.9876	NaN	0.9862	0.9860
14	NaN	0.9879	0.9872	0.9866	0.9859	0.9853
15	NaN	0.9876	0.9868	0.9862	0.9852	0.9843
16	NaN	0.9869	0.9860	0.9853	0.9841	0.9828
17	NaN	0.9855	0.9845	0.9842	0.9821	0.9798

List of References

(). *MAR101: Basic Nonlinear Analysis using MArc and Mentat*.

Anssari-Benam, A., Legerlotz, K., Bader, D. and Screen, H. (2012 July). Letter to the editor: On the specimen length dependency of tensile mechanical properties in soft tissues: Gripping effects and the characteristic decay length. *Journal of Biomechanics*, vol. 45, pp. 2481–2482.

Beers, K. (2006). *Numerical Methods for Chemical Engineering: Applications in MatLab*. Cambridge University Press, Cambridge, UK.

Besnard, G., Hild, F. and Roux, S. (2006 December). "finite element" displacement fields analysis from digital images: Application to portevin-le chatelier bands. *Experimental Mechanics*, vol. 46, pp. 789–803.

Blanchard, B. and Fabrycky, W. (1990). *Systems Engineering and Analysis*, vol. 4. Prentice Hall Englewood Cliffs, NJ.

Cabrera, M.S., Oomens, C., Bouten, C., Bogers, A., Hoerstrup, S. and Baaijens, F. (2013). Mechanical analysis of ovine and pediatric pulmonary artery for heart valve stent design. *Journal of biomechanics*, vol. 46, no. 12, pp. 2075–2081.

Chang, Y., Tsheng, W. and Tsao, R. (2005 September). Application of combined feasible-direction method and genetic algorithm to optimal planning of harmonic filters considering uncertainty conditions. *IEE Proceedings - Generation, Transmission and Distribution*, vol. 152, no. 5, pp. 729–736.

Cupido, B., Peters, F. and Ntusi, N. (2016 January). An approach to the diagnosis and management of valvular heart disease. *South African Medical Journal*, vol. 106, no. 1, pp. 39–42.

Garbowski, T., Maier, G. and Novati, G. (2012). On calibration of orthotropic elastic-plastic constitutive models for paper foils by biaxial tests and inverse analysis. *Struct Multidisc Optim*, pp. 111–128.

GmbH, L. (nd). 2d-/3d stereo dic. Accessed 20 October 2018. Available at: `https://www.lavision.de/en/products/strainmaster/2d-stereo-dic/index.php`

Hamid, M.S., Sabbah, H.N. and Stein, P.D. (1985). Finite element evaluation of stresses on closed leaflets of bioprosthetic heart valves with flexible stents. *Finite Elements in Analysis and Design*, vol. 1, no. 3, pp. 213–225.

Humphrey, J. (2003 January). Review paper: Continuum biomechanics of soft biological tissues. *Proceedings: Mathematical, Physical and Engineering Sciences*, vol. 459, no. 2029, pp. 3–46.

Jekel, C., Venter, G. and Venter, M. (2016 May). Obtaining a hyperelastic nonlinear othotropic material model via inverse bubble inflation analysis. *Structural and Multidisciplinary Optimization*, vol. 54, no. 4, pp. 927–935.

Jiang, H., Campbell, G. and Xi, F. (2005). Measurement and reconstruction of the leaflet geometry for a pericardial artificial heart valve. *Medical engineering & physics*, vol. 27, no. 2, pp. 175–180.

Jimenez, M., Brown, T. and Brand, R. (1989). The effects of grip proximity on perceived local in vitro tendon strain. *Journal of Biomechanics*, vol. 22, pp. 949–955.

Kheradvar, A., Groves, E.M., Dasi, L.P., Alavi, S.H., Tranquillo, R., Grande-Allen, K.J., Simmons, C.A., Griffith, B., Falahatpisheh, A., Goergen, C.J. *et al.* (2015). Emerging trends in heart valve engineering: part i. solutions for future. *Annals of biomedical engineering*, vol. 43, no. 4, pp. 833–843.

Kumar, N. and Rao, V. (2016 January). Hyperelastic mooney-rivlin model: Determination and physical interpretation of material constants. *MIT International Journal of Mechanical Engineering*, vol. 6, no. 1, pp. 43–46.

Lanir, Y. (1982). Constitutive equations for fibrous connective tissues. *Journal of Biomechanics*, vol. 16, no. 1, pp. 1–12.

Legg, M., Mathews, E. and Pelzer, R. (2012). The design and development of a stented tissue mitral and aortic heart valve replacement for human implantation. *Cardiovascular Journal of Africa*, vol. 23, pp. 126–130.

LePage, W. (2018). digitalimagecorrelation.org, a practical guide to DIC . Accessed 20 October 2018.
Available at: `http://digitalimagecorrelation.org/`

Martins, P., Jorge, R. and AJM, F. (2006). A comparative study of several material models for prediction of hyperelastic properties: Application to silicone-rubber and soft tissues. *Strain*.

Meunier, L., Chagnon, G., Favier, D., Orgéas, L. and Vacher, P. (2008 May). Mechanical experimental characterisation and numerical modelling of an unfilled silicone rubber. *Polymer Testing*, vol. 27, pp. 765–777.

Mooney, M. (1940). A theory of large elastic deformations. *Journal of Applied Physics*.

Pahl, G. (2001). *Engineering Design: a Systematic Approach*. 2nd edn. Springer, London.

Panda, S. and Buist, M. (2018). A finite, nonlinear, hyper-viscoelastic model for soft biological tissues. *Journal of Biomechanics*.

Pioletti, DP Rakotomanana, L. (2000 April). Non-linear viscoelastic laws for soft biological tissues. *European Journal of Mechanics A/Solids*, vol. 19, pp. 749–759.

Research, V. and Development, I. (2008 November). Dot design optimization tools. Technical Brochure Available At: www.vrand.com/sites/default/files/pub/dot5.0.pdf.

Reu, P. (2012*a*). Stereo-rig design: Camera selection-part 2. *Experimental Techniques*, vol. 36, pp. 3–4.

Reu, P. (2012*b*). Stereo-rig design: Creating the stereo rig layout-part 1. *Experimental Techniques*, vol. 36, pp. 3–4.

Reu, P. (2013*a*). Stereo-rig design: Lens selection-part 3. *Experimental Techniques*, vol. 37, pp. 1–3.

Reu, P. (2013*b*). Stereo-rig design: Lighting-part 5. *Experimental Techniques*, vol. 37, pp. 1–2.

Reu, P. (2013*c*). Stereo-rig design: Stereo angle selection-part 4. *Experimental Techniques*, vol. 37, pp. 1–2.

Ridge, M. and Wright, V. (1965). The rheology of skin - a bioengineering study of the mechanical properties of human skin in relation to its structure. *Br. J. Derm*, vol. 77, pp. 639–649.

Ridge, M. and Wright, V. (1966*a*). The directional effects of skin. *J. Invest. Derm*, vol. 46, pp. 341–346.

Ridge, R. and Wright, V. (1966*b*). Mechanical properties of skin: a bioengineering study of skin structure. *Journal of Applied Physiology*, vol. 21.

Rivlin, R. (1948). Large elastic deformations of isotropic materials iv: Further developments of the general theory. *Philosophical Transactions of the Royal Society of London*, vol. 241, no. A, p. 379.

Roy, C. (1880). The elastic properties of the arterial wall. *Philosophical Transactions of the Royal Society of London*, vol. 99, no. B, pp. 1–31.

Sanjeevi, R., Somanathan, N. and Ramaswamy, D. (1982). A viscoelastic model for collagen fibres. *Journal of Biomechanics*.

Smooth-On (nd). *Ecoflex Series: Super-Soft, Addition Cure Silicone Rubbers*. Smooth-On, 5600 Lower Macungie Road, Macungie, PA, 18062, USA. Manufacturer Datasheet.

Strumpf, R., Humphrey, J. and Yin, F. (1993 March). Biaxial mechanical properties of passive and tetanized canine diaphragm. *The American Physiological Society*, , no. H, pp. 469–468.

Sun, W., Sacks, M. and Scott, M. (2005). Effects of boundary conditions on the estimation of the planar biaxial mechanical properties of soft tissues. *Journal of Biomechanical Engineering*, vol. 127, pp. 709–715.

Sutton, M., Cheng, M., Peters, W., Chao, Y. and McNiell, S. (1986 August). Application of an optimized digital correlation method to planar deformation analysis. *Image and Vision Computing*, vol. 4, no. 3, pp. 143–150.

Swanson, S., Christensen, L. and Ensign, M. (1985). Large deformation finite element calculations for slightly compressible hyperelastic materials. *Computers and Structures*, vol. 21, no. 1/2, pp. 81–85.

Tillquist, M.N. and Maddox, T.M. (2011). Cardiac crossroads: deciding between mechanical or bioprosthetic heart valve replacement. *Patient preference and adherence*, vol. 5, p. 91.

Topal, U. and Uzman, U. (2008). Strength optimization of laminated composite plates. *Journal of Composite Materials*, vol. 42, no. 17, pp. 1731–1746.

Treloar, L. (1975). *The Physics of Rubber Elasticity*. 3rd edn. Oxford University Press.

Vacher, P., Dumoulin, S., Morestin, F. and Mguil-Touchal, S. (1999). Bi-dimensional strain measurement using images. *Proc Instn Mech Engrs*.

Veronda, D. and Westmann, R. (1970). Mechanical characterization of skin - finite deformations. *Journal of Biomechanics*, vol. 3, pp. 111–124.

Viljoen, D. (). Characterising material models for silicone-rubber using an inverse finite element updating method. M.Ing Thesis.

Vito, R. (1980 February). The mechanical properties of soft tissues - i: A mechanical system for bi-axial testing. *Journal of Biomechanics*, vol. 13, pp. 947–950.

Welt, F., Davidson, M. and Eisenhauer, A. (2012 August). The transcatheter valve revolution, time for a compensatory pause. Editorial.

Wertheim, M. (1847 January). Memoire sur l'eastocote et la cohesion des principaux tissues du corp humain. *Ann. Chim. Phys.*, vol. 21, pp. 385–414.

Yoganathan, A., He, Z. and Jones, C. (2004). Fluid dynamics of heart valves. *Annual Review of Biomedical Engineering*, vol. 6, pp. 311–362.

Zisis, T., Zafiropoulou, V. and Giannakopoulos, A. (2015 March). Evaluation of material properties of incompressible hyperelastic materials based on instrumented indentation of an equal bi-axial prestretched substrate. *International Journal of Solids and Structures*, vol. 64, no. 65, pp. 132–144.